Experimental and Numerical investigations of Cantilever Beam Tests in floating Ice Covers

Åse Ervik

MASTER'S THESIS

Experimental and numerical investigations of cantilever beam tests in floating ice covers

Author:
Åse ERVIK

Supervisors:
Kjell H. HOLTE (NTNU)
Knut V. HØYLAND (NTNU)
Aleksey MARCHENKO (UNIS)

Trondheim, June 2013

Abstract

Offshore activity in Arctic waters has become a propelling interest in the industry, bringing new challenges for structural design. Structures situated in the Arctic ocean must withstand loads from ice, amongst other challenges such as remoteness, low temperatures and harsh weather. Floating ice covers can crush or break when interacting with offshore structures. For sloping structures, ice mostly fails when bending, making the *flexural strength* the key parameter. The objective of this thesis was to investigate the cantilever beam test, for determining flexural strength of sea ice covers. Special emphasis was given to the impact of spatial variations of elastic modulus through the ice thickness on flexural strength.

Two scientific expeditions were designed and executed for this work. The first expedition went to Svea bay in Van Mijenfjorden on Spitsbergen, between the 05th and 16th of March 2013. The second expedition was performed on the research vessel Lance, travelling in the Barents sea south east of Edgeøya in the Svalbard archipelago, between the 25th of April and the 04th of May.

Applied bending moments for cold and warm ice seems to be similar and independent of temperature and the size of the beam. Because of this; previous flexural strength calculations have not taken into account variations of ice properties in the vertical direction. Stress fields have been assumed to be linearly distributed across the ice thickness, independent of the type of ice. Experimental results form the work presented in this thesis shows that; the elastic modulus seems to variate through the ice thickness in the same manner as the temperature. For cold ice the effect of this is that local stresses in the top ice layer and hence the flexural strength is highly underestimated.

The main importance of these findings for structural design seems to be the failure mode in sea ice. The work presented in this thesis endorse the appearance that cold ice is brittle and warm ice is ductile or quasi-brittle.

Additionally, the effect of the water support was studied by employing the *Winkler foundation*. Numerical analysis showed that the flexural strength including the Winkler foundation was within 99% of the flexural strength neglecting the water support. This indicates that the water foundation can be neglected from flexural strength calculations rightfully.

ii

Sammendrag

Aktiviteter i arktiske farvann er et hett. Dimensjonering av konstruksjoner for arktiske farvann fører med seg en rekke utfordringer. Deriblant er vær og klima, tilgjengelighet og laster fra sjøis. Konstruksjoner som befinner seg i isbelagte farvann må kunne motstå laster fra is som både knuses og brekker. For skrå strukturer (sloping structures) brytes isen ved bøying og for denne typen konstruksjoner er isens *bøyestyrken* den viktigste parameteren. Hovedpoenget med denne oppgaven er å studere utkragerbjelke-testen, som brukes til å bestemme bøyestyrken i sjøis. Det er lagt spesielt vekt på hvordan variasjoner av fysiske egenskaper og E-modul over istykkelsen påvirker bøyestyrken i sjøis.

To vitenskaplige ekspedisjoner ble planlagt og gjennomført i forbindelse med dette arbeidet. Den første ekspedisjonen ble gjennomført mellom 05. og 16. mars 2013 til sjøisen i Svea innerst i Van Mijenfjorden på Spitsbergen. Den andre ekspedisjonen fant sted på forskningsskipet Lance i perioden fra 25. april til 04. mai, skipet seilte fra Longyearbyen til sør-øst for Edgeøya i Barentshavet.

Bøyemomentet som skal til for å brekke en isbjelke er tilsynelatende det samme for varm og kald is, samt bjelker av ulik størrelse. På grunn av dette har tidligere beregninger av bøyestyrken i is ikke tatt høyde for at egenskaper ved isen varierer over tykkelsen og hvordan dette påvirker spenningsfordelingen. Tradisjonelt er det blitt antatt at isen er homogen og at spenningsfordelingen over tverrsnittet er lineær. Eksperimentielle resultater fra arbeidet med denne oppgaven har vist at stivheten i isen (E-modulen) variere over istykkelsen likt med temperaturen. For kald is er det blitt vist at denne variasjonen fører til høye strekkspenninger i den øvre delen av isbjelken og at den lineære spenningsfordelingen gir for lav bøyestyrke.

For strukturdesign er hovedkonsekvensen av at E-modulen er temperaturavhengig at spenningsfordelingen igjennom istykkelsen endres. I andre rekke underbygger disse funnene at kald is er sprøere enn varm is.

I tillegg er betydningen av kreftene fra vannet på bøyestryken undersøkt, ved å innkludere et elastisk fundament (Winkler fundamentet). Fra numeriske beregninger er det blitt vist at bøyestyrken med Winkler fundamentet er 99 % av bøyestryken hvor vannet er utelatt fra analysen. Dermed utgjør vannfundamentet et ubetydelig bidrag til det totale momentet og kan utelukkes ved beregninger av bøyestyrken.

Contents

List of Figures

List of Tables

Preface

This thesis will be submitted for the degree of Master of Science and Technology (Sivilingeniør), concluding my education at NTNU. It is the result of my work during the spring semester of 2013, formally at the Department of Structural Engineering, under the supervision of professor Kjell H. Holte, to whom I am grateful for making this thesis possible. The work of this thesis was carried out on the University Centre in Svalbard, under the supervision of professor Knut V. Høyland (NTNU, at the Department of Civil and Transport Engineering) and professor Aleksey Marchenko (UNIS, at the Department of Technology), to whom I am grateful for the support and guidance they have generously provided.

I want to thank the SMIDA-group participants; Dr. Marina Karulina, Dr. Evgeny Karulin, Dr. Alexandr Sakharov, Dr. Peter Christyakov and PhD student Aleksey Vakulenko for excellent guidance and cooperation on the expedition to Svea. I also want to thank UNIS students (from the course AT-211, spring 2013) participating on the expedition to Svea bay and the Barents sea for their excellent hands on work.

A great thanks to PhD student Torodd Nord at the Department of Civil and Transport Engineering, for valuable discussions and suggestions. Additionally, logistics and safety could not have been handled without the guidance of Jomar Finseth, adjunct professor UNIS.

Finally, I want to thank my brother Åsmund Ervik for his knowledge of LaTeX, and my parents Anne Marie and Alf Åsmund Ervik for arousing an interest for cold climates, supporting my decision on moving to the high Artic.

I also wish to acknowledge the contributions to this work from the Sustainable Arctic Marine and Coastal Technology (SAMCoT) project, led my Professor Sveinung Løset at NTNU.

Åse Ervik
June 10, 2013

1 Introduction

Offshore activity in Arctic waters has become a hot topic in recent years, bringing new challenges for structural design. Structures situated in the Arctic ocean must withstand loads from ice, amongst other challenges such as low temperatures and harsh weather. Floating sea ice covers may crush or break when interacting with offshore structures, so the strength of the ice is important for dimensioning ice loads. For sloping structures, ice mostly fails when bending, making the flexural strength the key parameter. This leads to the topic of this thesis, namely the flexural strength of sea ice. Flexural strength is a material property, but for ice it strongly depends on e.g. temperature, salinity, porosity and elastic modulus.

Several authors have previously studied sea ice strength. Høyland (2009) showed that there are large spatial variations of physical properties through the ice thickness, particularly for cold ice. Timco and O'Brien (1993) have shown that flexural strength decreases with increasing brine fraction. However, few authors have yet studied how spatial variations of mechanical properties (strength and elastic modulus) affect the flexural strength. Kerr and Palmer (1972) published an article where a variable elastic modulus was used to express the horizontal stress distribution through the ice thickness. They showed theoretically that this made a significant increase of the stress in the top ice layer, but lacked experimental data to compare against.

The main objective of this thesis is to study how spatial variations of elastic modulus and strength throughout the ice thickness affects the average flexural strength of a sea ice cover, and how this relates to physical ice properties. Previous studies have neglected forces from the water supporting the ice sheet in the flexural strength calculations. In this thesis, the significance of the water support will be studied.

Experimental work has been a significant part of the present work. Two scientific expeditions on sea ice were designed and executed together with the SMIDA-group and UNIS students (from course AT-211). The first expedition went to Svea bay in Van Mijenfjorden on Spitsbergen, between the 05th and 16th of March 2013. The second expedition was performed on the research vessel Lance, travelling in the Barents sea south east of Edgeøya in the Svalbard archipelago, between the 25th of April and the 04th of May. Six cantilever beam tests, temperature, salinity, porosity and uni-axial compression tests were performed on each expedition.

2 Theory

Contents

The flexural strength in sea ice is a subject which has been extendedly investigated, Marchenko (2011). Timco and Weeks (2009) gives a review of general ice properties. The main objective of this thesis is flexural strength, studied with the cantilever beam method. The flexural strength of floating ice covers is the main interest for sloping structures. It should already here be stressed that the term property is vague, as measurements in the field are strongly dependent on the natural environment, the time and indeed the test set up itself.

For the investigation of flexural strength there are three main methods, namely an in-situ cantilever beam test, a simple three point bending test and a 4 point bending test (seen in figure 17). According to recommendations made by Kämäräinen (1993), an *in-situ* cantilever beam test is preferred for the investigation of flexural strength in sea ice. Flexural strength formulas and calculations are based on a cantilever beam geometry, seen in figure 1.
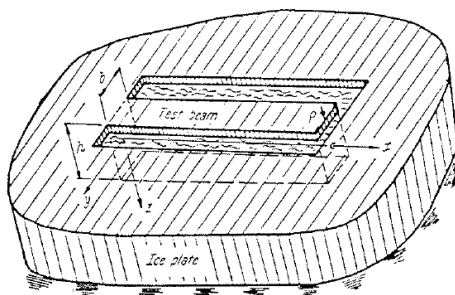
Figure 1: Set up in-situ test. From page 80 Kämäräinen (1993)

Due to the dependency between physical and mechanical properties in sea ice an investigation of physical properties such as salinity, ice structure, temperature and porosity is done together with strength and stiffness. Possible effects from the physical properties on the mechanical properties are described in the next section.

2.1 Physical properties

Here we give a brief review of physical properties that may affect strength in first year (FY) level sea ice, starting on the atomic level with the ice crystal, proceeding towards the structural scale of the ice model set-up.
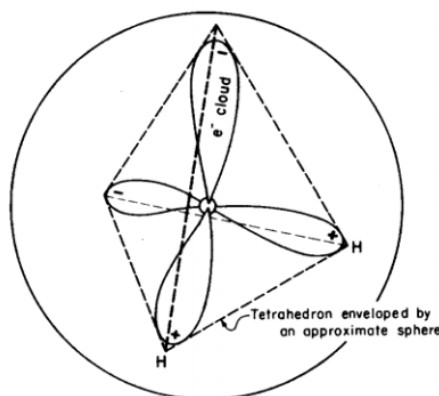
Figure 2: The water molecule consist of the oxygen core located in the centre, two positively charged hydrogen protons and two negatively charged electron clouds (Marchenko, 2012).

2.1.1   The ice crystal

Ice is the solid form of H_2O. The strong atomic bonds in the H_2O molecule are two covalent atomic bondings. The atoms are oriented as shown in figure 2 making up a tetrahedron. The weak bonds between molecules are the bonds that determine the structure of an ice crystal or grain. The weak bonds between the H_2O molecules, are know as hydrogen bonds. These connect the small positive proton in hydrogen, to the highly electronegative[1] oxygen atom. One H_2O molecule can in total connect to four other H_2Os. When connecting these tetrahedrons a hexagon emerge, see figure 3. The crystal structure of ice is hexagonal, the proper term for this ice is therefore hexagonal ice. According to Petremko and Whitworth (1993) ice is formed for temperatures between $0\,^{\circ}C$ and $-80\,^{\circ}C$, which is basically what we have on earth. Further in this thesis ice simply refers to hexagonal (Ih) ice.

The hexagon shown in figure 3 is an open structure made up from tetrahedrons connected by hydrogen bondings. By removing heat energy, water transforms into solid ice, where all H_2O molecules align from the disordered configuration found in water employing more space than the liquid form of H_2O. As a result water has a higher density than ice and will float.[2] Off course there exists dislocations and defects in the ice lattice, which is a unit cell of the ice crystal. These imperfections affect the mechanical behaviour and strain in ice (treated in section 2.2). Bernal and Fowler (1933) suggested several rules regarding the location of hydrogen atoms in hydrogen bondings. Dislocations and defects are present when a rule is broken. The main rules state the following:

---

[1]Electronegativity is the ability of an atom to attract other electrons to itself. Oxygen and fluorine are examples of highly electronegative atoms.(Zumdahl, 2009)

[2]Ice is approximately 9 % less dense than water, fresh water has its maximum density at $4\,^{\circ}C$.(Zumdahl, 2009)
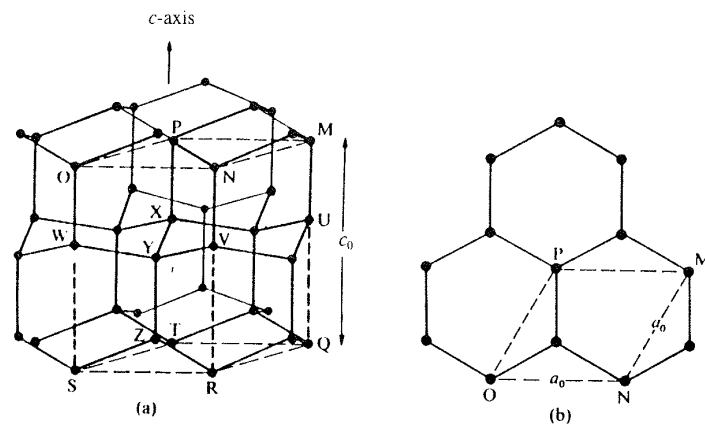
Figure 3: Here the hexagonal structure in ice is displayed. The vertical axis is the C-axis. The basal planes are the horizontal planes, displayed in (b). (Hobbs, 1974)

1. The H_2O in ice is similar to one in the free gas phase.

2. Ths H_2O molecule is oriented such that the two hydrogen protons are located toward two out of four oxygen atoms in the tetrahedron.

3. Only one hydrogen atom is located between two oxygen.

In the book of Hobbs (1974) figure 3 can be found, illustrating the anisotropy of the ice crystal. By observing the hexagon it can be seen that the atomic structure consists of planes separated by half the C_0 distance, orientated in the C-axis direction. The densely packed planes are called basal planes.

Sea ice is a polycrystalline material. In general the first ice will form when the water temperature is below the freezing point and there exists nuclei for the ice to form on, such as snow or impurities. According to Kämäräinen (1993) initially the first ice-sheet is assumed to form in the horizontal direction of the water. Observations of the top sheet of ice has revealed grains of random C-axis orientation in all 3 dimensions. This ice is called granular ice and is shown in figure 4; crystal dimensions are of the order of millimetres. As the initial ice cover is formed the ice starts growing as heat is transported from the warm water to the cold air, this is called the transition zone. Favoured crystals have vertical basal planes coinciding with a horizontal c-axis. This corresponds to orienting the basal planes in the direction of the heat flow. It is shown in figure 5, for fresh water ice, that certain grains become larger as the ice thickness increases, indicating a horizontal c-axis orientation. The grain size is also affected by the weather and water conditions such as tidal actions, this may be one reason why grains found in sea ice are often smaller than grains found in fresh water ice.
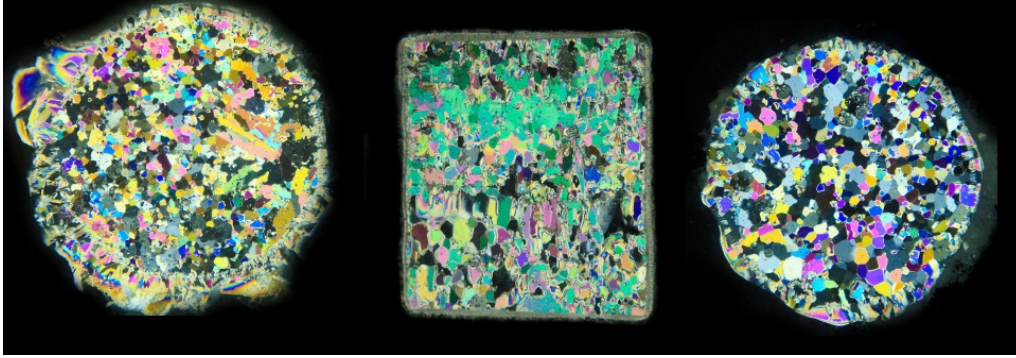
Figure 4: Granular ice from an initial sea ice cover taken from the Van Keulen fjord located south of the Van Mijen fjord on Spitsbergen. Horizontal top section diameter 70mm, vertical section length 100mm and bottom horizontal section diameter 70mm. (Ervik Åse, 2012)
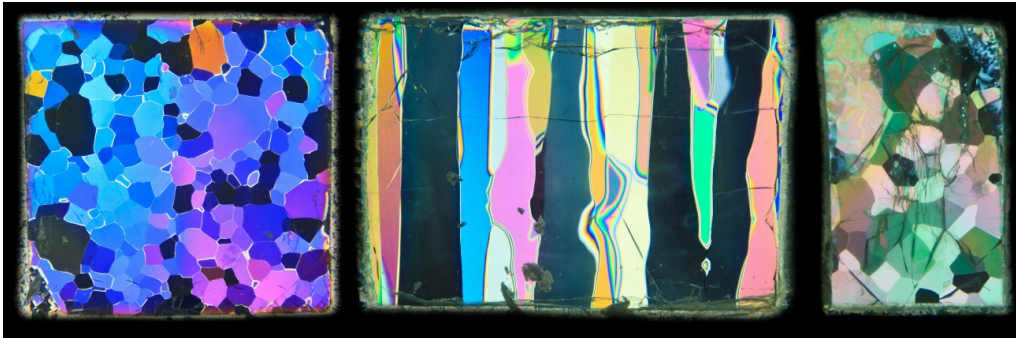
Figure 5: Columnar fresh water ice. Horizontal top section, vertical section and bottom horizontal section, lengths of sections 100mm. (Ervik Åse, 2012)

2.1.2   Brine and gas porosity

Salt is a natural substance in sea ice. Different salts give different crystallization temperatures (eutectic temperatures). According to Kämäräinen (1993) sea salt or $NaCl \cdot 2H_2O$ has an eutectic temperature of $-21.1\,^{\circ}C$. Due to the low freezing temperature of salt, it rarely appears as solid crystals in level ice, but is more likely to be found as *brine*. Brine is a slushy mixture of water and salt which is trapped inside the ice. Brine pockets are shown in figure 6. The brine volume is the fraction of the ice occupied by salt and water, determined by salinity, density and temperature.

Another factor that influences the ice structure is the content of gas, i.e. gas porosity. According to Kämäräinen (1993) gases get trapped inside the ice because of wave action during freezing and gas content in the water.

The brine and gas porosities are found from the temperature, salinity and ice density. The derivation of the porosities for ice colder than $-2\,^{\circ}C$ were made by Cox and Weeks (1983), the porosity for ice warmer than $-2\,^{\circ}C$ by Leppäranta and Manninen (1988).

The freezing temperature is given by the brine salinity S_b:
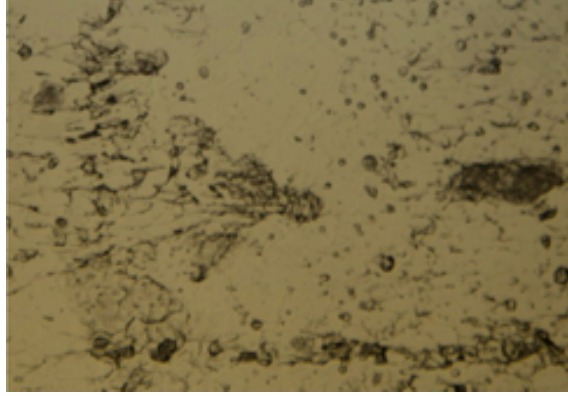
Figure 6: Brine pocket. (Ervik Åse, 2012)

$$T_f = -0.0575S_b + 1.710523^{-3}(S_b)^{3/2} - 2.154996^{-4}(S_b)^2 \tag{1}$$

Leppäranta and Manninen (1988) derived the following formulas for the brine and gas porosities of ice warmer than $-2\,°C$:

$$\nu_b = \frac{\rho_i S_i}{S_b \rho_b} \tag{2}$$

$$\nu_a = 1 - \frac{\rho_i}{\rho_{pi}} + \nu_b[\frac{\rho_b}{\rho_{pi}} - 1] \tag{3}$$

Ice with $-22.9\,°C < T < -2\,°C$ has the following brine and gas porosity, according to Cox and Weeks (1983):

$$\nu_b = \frac{\rho_i S_i}{F_1(T)}, \tag{4}$$

$$\nu_a = 1 - \frac{\rho_i}{\rho_{pi}} + \rho_i S_i \frac{F_2(T)}{F_1(T)}, \tag{5}$$

where the following properties: T temperature, ρ_i ice density and S_i ice salinity are measured. ρ_b brine density, S_b brine salinity, ρ_{pi} pure ice density, and $F_1(T)$ and $F_2(T)$ were estimated by Cox and Weeks (1983) and are given as:

$$F_1(T) = -4.732 - 22.45T - 0.6397T^2 - 0.01074T^3 \tag{6}$$

$$F_2(T) = 9899 + 1309T + 55.27T^2 + 0.716T^3 \tag{7}$$

The pure ice density ρ_{pi} was estimated by Pounder (1965):

$$\rho_{pi} = 0.9168(1 - 1.53E - 4T) \tag{8}$$

The brine salinity is found by the equation in Cox and Weeks (1983):

$$\rho_b = 1 + 0.0008 S_b, \tag{9}$$

where the brine salinity can be estimated from temperature, salinity and density, according to tables in Assur (1958).

2.1.3   A sea ice cover

This section links physical ice properties together and shows how physical properties varies across the thickness of a sea ice cover. A sea ice cover changes through a season, regulated by the thermal heat transfer between the water, ice and air. The texture, salinity and temperature in the ice sheet changes as the ice thickness increases and decreases. According to Høyland (2009) new ice may grow in the top, interior and the bottom of the ice sheet. Ice growth in the bottom is often the dominating mechanism. Høyland (2009) and Sinha and Nakawo (1981) only consider ice growth in the lower layer of the ice when consider the heat flux balance for determining the maximum ice thickness, also neglecting solar radiation. The ice growth and thickness may be estimated by Stefan's Law:

$$h^2 = h_0^2 + \frac{2k}{\rho l} \sum_n (T_f - T_{is}) \tag{10}$$

where h and h_0 is the current and the initial ice thickness respectively, k is the thermal conductivity of ice, ρ is the ice density, l is the latent heat, T_f is the freezing temperature, T_{is} is the daily average ice surface temperature and n is the number of days. If the ice surface temperature is not accessible, the air temperature T_a and the number of freezing degree days (FDDs) in the timespan (t_0, t), is used. FDD is defined as:

$$FDD = \int_{t_0}^{t} \max(0, T_f - T_a) \mathrm{dt} \tag{11}$$

If an empirical coefficient ω is introduced then Stefan's Law becomes:

$$h^2 = h_0^2 + \omega \frac{2k}{\rho l} FDD \tag{12}$$

Although the ice mainly grows in the bottom, flooding, rain or snow melting causes the ice to grow on the top. According to Høyland (2009) ice formed from flooded sea ice will have high salinity whereas ice from rain or snow melt will be fresh and porous. Interior melting/freezing occurs when brine melts/freezes. A secondary effect is brine drainage and desalination of ice. The ice melts when brine drains towards a

positive temperature gradient consuming heat from the warmer ice, whereas when the temperature gradient is negative new ice is formed and heat is released.

The heat flux balance in the lower part of a growing ice sheet is given by:

$$q_{ocean} + q_i + q_{lat} = 0 \tag{13}$$

where q_{ocean} is the heat flux from the water, q_i is the heat conduction from the ice to the air, q_{lat} is the latent heat released from the ice as it grows.

$$q_i = -k\frac{\partial T(z)}{\partial z} \quad q_{lat} = \rho l\frac{\text{dh}}{\text{dt}} \tag{14}$$

where k is the thermal conductivity, $\frac{\partial T(z)}{\partial z}$ is the temperature gradient, ρ the ice density, l the latent heat and $\frac{\text{dh}}{\text{dt}}$ is the ice growth velocity.

If the temperature profile $T(z)$ and ice thickness Δh are measured, the average oceanic flux over a time period $t = \sum \Delta t_j$ can be estimated as follows:

$$q_{ocean} = k\frac{\partial T(z)}{\partial z} - \rho l\frac{\text{dh}}{\text{dt}} \longleftrightarrow q_{ocean} = [k\sum(\frac{\Delta T}{\Delta z})_j \Delta t_j - \rho l \Delta h]/\sum \Delta t_j \tag{15}$$

If the ocean heat flux is neglected the maximum ice thickness can be estimated according to:

$$h_{max} = \frac{k}{\rho l}\frac{\Delta T}{\Delta z}\Delta t \tag{16}$$

According to Høyland (2009) the ice thickness depends on several other factors than the heat balance: meteorological conditions (air temperature, wind and snow and solar radiation), ocean conditions (velocity, tides, salinity and temperature) and also physical constraints of ice movement such as bay topology or islands. Høyland (2009) explains for instance the relatively thick ice cover found in Van Mijenfjorden, compared to other western fjords on Spitsbergen, by the low air temperature, snow depth and oceanic flux and the confining effect of Akseløya.

A sea ice cover is a polycrystalline material and it can be separated into different zones. Kämäräinen (1993) divides the ice structure into the primary ice, the transition zone and the secondary ice, where most of the ice cover consists of secondary ice. The texture of a typical sea ice sample taken in Van Mijenfjorden is shown in figure 4; as mentioned in section 2.1.1 crystal dimensions were in the order of millimetres. The main ice texture is determined from the secondary ice. According to Høyland (2009) the ice texture typically found in the Van Mijenfjorden on Svalbard had a columnar structure with a vertical crystal length of more than $0.1m$, and a diameter of up to $0.03m$. C-axis orientations in the horizontal plane were random.

Kämäräinen (1993) uses Michel and Ramseiers classification of natural ice to distinguish sea ice textures. According to this classification the sea ice structure typically found in Van Mijenfjoden is S2 structure. S2 ice has a columnar crystal structure with crystals elongated in the vertical direction and randomly distributed c-axes in the horizontal direction. According to Lemaitre and Chaboche (1990) S2 ice is transversely isotropic, the elastic characteristics are invariant for all pairs of directions symmetric with respect to the vertical axis, the material is isotropic in planes normal to the vertical axis.

Both temperature and salinity profiles in sea ice covers varies in the vertical direction. The temperature distribution across the ice thickness is regulated by the air and water temperature. Typical temperature profiles found in Van Mijenfjorden in Svea bay are shown in figure 7. Temperature profiles found early in the winter varies strongly from the cold air-surface to the warm water, profiles found late in winter are uniform when air temperatures are higher.
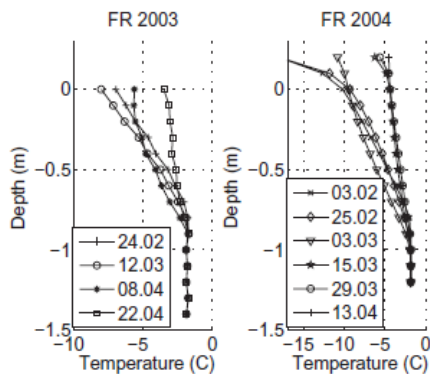
Figure 7: Temperature profiles found in Van Mijenfjoden at Svea in March 2004. Høyland (2009).

A large number of observations of salinity profiles reveals that salinities seems to be higher in the top and bottom ice boundaries. Kämäräinen (1993) explains this as due to brine expulsion, gravity drainage and flushing, all effects that force salt to migrate out of the ice through brine channels to the ice-water surface and the air-ice surface, desalinating the ice texture. Sinha and Nakawo (1981) measured salinity profiles at Eclipse Sound in Canada at intervals of 2 weeks in 1977-78, they obtained the salinity profiles seen in figure 8. If salinity is found to be lower in the top layers this may coincide with snow melting or rain.

Finally, tides influence a sea ice cover and in particularly land fast sea ice. Gabrielsen et al. (2008) label ice frozen to the shore the *ice foot*, which is blocks of ice fixed to the ground, formed early in the season by tides and water spray. At a certain distance from the shore the ice is unaffected by the land and floats freely; this ice is labelled *level ice*. The zone inbetween the fixed and the free ice is subjected to tidal forces significant enough to create tidal cracks; this ice is called *coastal ice*. Gabrielsen et al. (2008) measured physical and mechanical properties of coastal and level ice, and found that level ice had a higher density, salinity and brine fraction
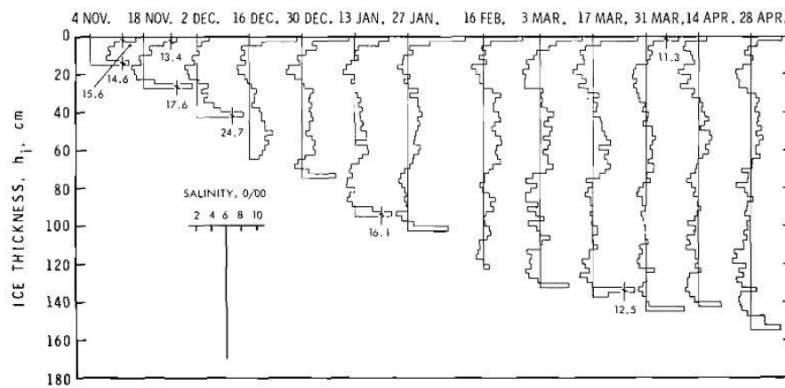
Figure 8: Salinity profiles in the ice at Eclipse Sound taken at intervals of 2 weeks during the winter of 1977-78. The vertical line represents a reference value of 6 parts per thousand. Sinha and Nakawo (1981).

but lower gas fraction and total porosity. Level ice was stiffer but significantly more viscous than coastal ice. This thesis will focus on level ice, at a certain distance from the shore line where it is unaffected by the land.

2.2   Mechanical properties

The mechanical behaviour of pure ice has been widely studied. Sinha (1983) and Sanderson (1988) investigated the mechanical behaviour of ice by decomposing strains. The reason for doing that, is that ice is not a purely elastic, viscous or plastic material. When a load is applied to an ice sample, it responds elastically and simultaneously starts to creep i.e. it behaves time-dependently. The reason creep always plays a role is that operational temperatures in ice engineering, often are close to the melting temperature. (Lemaitre and Chaboche, 1990).

In this section an attempt is made to distinguish the elastic and time-dependent mechanical properties in ice. This is done through a decomposition of the strains. Mechanical properties are further related to physical properties of ice, discussed in section 2.1. It is however stressed that it is the elastic mechanical properties that are the main scope of this thesis.

2.2.1   General

Sinha (1981) decomposes strain into three macroscopically observable strain components, namely a pure elastic strain, ϵ_e, a delayed elastic strain, ϵ_d and a permanent or viscous strain, ϵ_v. The total strain, ϵ_t, is the sum of ϵ_e, ϵ_d and ϵ_v:

$$\epsilon_t = \frac{\sigma}{E} + c_1 \frac{d_1}{d} (\frac{\sigma}{E})^2 [1 - \exp(-(a_T t)^b)] + \dot{\epsilon_{v_1}} t (\frac{\sigma}{\sigma^1})^n, \tag{17}$$

where E is the elastic modulus, $\dot{\epsilon_{v_1}}$ is the viscous strain rate for the unit or reference stress σ_1; d is grain size, d_1 is a constant corresponding to the unit reference grain size; c_1, b and n are constants; s is the stress component for the delayed elastic strain and a_T is the inverse relaxation time. Both $\dot{\epsilon_{v_1}}$ and a_T vary with temperature and are shown to have the same value for the activation energy.(Sinha, 1981)

The elastic strain or the recoverable strain $\epsilon_e = \frac{\sigma}{E}$ is time independent, according to Sinha (1981) this is due to atomic bond deformation of the ice grain. Upon removing the load, this deformation will be recovered. No dissipation is present in the purely elastic strain in equation 17, neither thermal dissipation (thermoelasticity) nor mechanical dissipation (viscoelasticity). The time dependent properties include both the recoverable elastic delayed deformation (viscoelastic) and the creep and permanent (viscoplastic) deformation. According to Sinha (1981) and Sanderson (1988) the delayed elastic deformation ($\epsilon_d = c_1 \frac{d_1}{d} (\frac{\sigma}{E})^2 [1 - \exp(-(a_T t)^b)]$) represents grain boundary sliding without permanent deformation. If a sample is compressed, grain boundaries are rearranged, the ice relaxes upon removing the load and restores its initial shape after a certain time. The permanent viscous deformation ($\epsilon_v = \dot{\epsilon_{v_1}} t (\frac{\sigma}{\sigma^1})^n$) represented mainly by grain dislocation movements, is called secondary creep. Dislocations may also pile up, leading to tertiary creep, micro cracks and ultimately failure. Creep is thus divided into primary, secondary (steady state) and tertiary (failure) creep.

2.2.2 Elastic properties

In engineering, the elastic strain is given by the nominal stress and the elastic modulus, $\epsilon_e = \frac{\sigma}{E}$. This strain is well suited for engineering applications when strains are relatively small and linear, following Hooke's law. For larger deformations and non-linear stress-strain curves, finite strains are better suited. One such strain is the Almani strain, with the deformed configuration as reference system.

Engineering strain:

$$\epsilon_e = \frac{l - l_0}{l_0} \tag{18}$$

Almani strain:

$$\epsilon_a = \frac{l^2 - l_0^2}{2l^2} \tag{19}$$

where l_0 is the initial length, l is the deformed length.

Compressive and tensile stresses are elastic properties. When a specimen is loaded by a tensile uni-axial force, the specimen length will increase and the cross section area will decrease; the opposite happens in compression. In engineering, nominal stress is defined as $\sigma = \frac{N}{A_0}$, where the stress is expressed according to the initial cross section area A_0. If deformations are large, nominal stress is not so useful because the force will be distributed over an area considerably larger (compression) or smaller (tension) than the initial area A_0. Stresses and strains are work conjugate, meaning that they must be expressed according to the same reference system, either the initial or deformed. Here uni-axial stress and strain is taken as the nominal value expressed according to the initial reference system, so that deformations are considered to be small and elastic.

2.2.3 Time-dependent properties

Stress, and also strength and failure, are all related to strain rate. Failure is either ductile, transitional or brittle; ice seems to experience all types of deformations depending on the loading, strain rate, temperature and ice texture. From equation 17, if the constants n and s are small, it can be shown that if t is small, indicating a high strain rate, the two last terms become small. Hence for high strain rates, elastic strain ϵ_e is the dominating strain. Sanderson (1988) collected data on the strength of pure ice loaded in tension and compression, with different strain rates and temperature. This plot (figure 9) coincides well with what was found from equation 17; namely that creep is significant up to a strain rate of 10^{-5} undergoing a transition to brittle failure for higher strain rates.
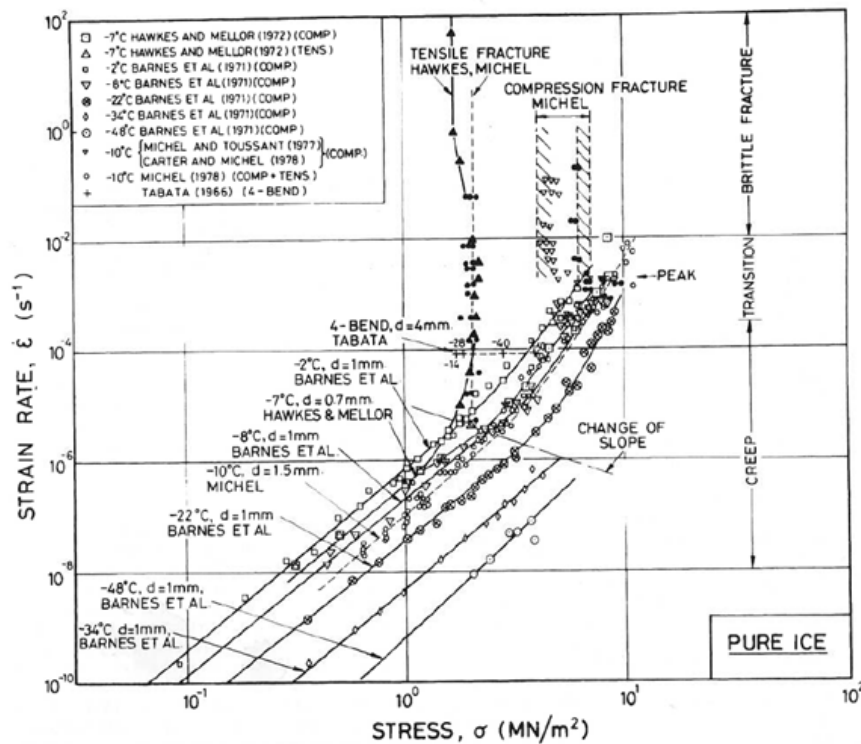
Figure 9: Uniaxial loading of pure polycrystalline ice. Below a strain rate of about $10^{-5}[s^1]$ creep occurs. For stresses exceeding 5-10MPa, a transition to brittle behaviour occurs. (Sanderson, 1988)

2.2.4   Strength or time-independent properties

The main objective of determining ice strength is to simulate how the ice fails in nature. *Strength* in this thesis refers to the stress at the elastic limit assuming the Von Mises' yield criteria is valid. For ice the elastic strength may coincide with the ultimate (failure) strength if the ice is brittle. Strengths considered in this thesis are:

* *compressive strength*, nominal uni-axial limit stress in compression

* *tensile strength*, nominal uni-axial limit stress in tension

* *flexural strength*, limit stress in bending

Uni-axial tests are used to determine uni-axial strengths and effective modulus from the stress-strain curve. Uni-axial strength of ice depends on the loading direction. Columnar S2 ice has grains that extends further in the vertical than the horizontal direction. Moslet (2007) did a review of a number of studies on the ratio between vertical and horizontal compressive strength, σ_v/σ_h. He found that the ratio ranged from 1.2 to 4.0 for S2 columnar sea ice, fitting well with differences in the physical properties in the horizontal and vertical direction. Timco and Frederking (1990) estimated full scale sea ice sheet strength from both horizontal and vertical compression samples, they collected a large amount of data and found a ratio of σ_v/σ_h ranging from 2.5 to 3.9.

Tensile and compressive strengths are additionally different. Schulson (1983) found a significant difference in nominal tensile- and compressive strength. The compressive strength is up to ten times the tensile strength at a strain rate of $10^{-3}[s^{-1}]$. Strain rate seems to affect the tensile strength to a lesser extent than compressive strength. The data in figure 10 was obtained from fresh water ice with grain size 1 mm and the ice was randomly orientated.
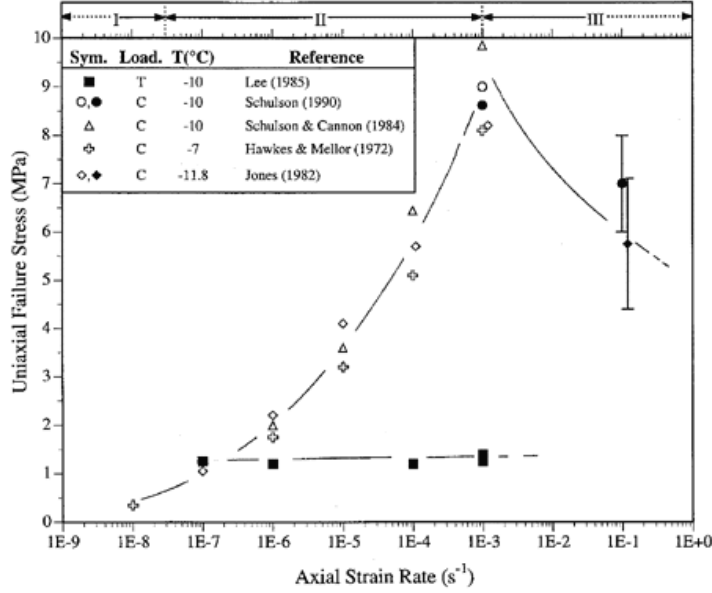
Figure 10: Tensile (T) strength and compressive (C) strength as function of the strain rate. Schulson (1983)

The uni-axial strengths shown in figure 10 were measured for fresh ice. Sea ice contains brine pockets and channels. These imperfections are not able to carry shear stresses and additionally they cause stress concentrations; reducing the strength (Sanderson, 1988).

Timco and Frederking (1990) related compressive strength to the total porosity volume and strain rate for both horizontal and vertical samples. The strain rate range for these equations was from $10^{-7}s^{-1}$ to $10^{-4}s^{-1}$. Above this strain rate, premature (brittle) failure of ice could occur (Timco and Frederking, 1990). They got the following equations for horizontal (equation 20) and vertical (equation 21) compressive strength:

$$\sigma_c^H = 37\dot{\epsilon}^{0.22}[1 - (\frac{\nu_T}{270})^{0.5}] \tag{20}$$

$$\sigma_c^v = 160\dot{\epsilon}^{0.22}[1 - (\frac{\nu_T}{200})^{0.5}] \tag{21}$$

Moslet (2007) also performed compressive test. This author used a nominal strain rate of $10^{-3}[s^{-1}]$, and found the following relations for compressive strength in the horizontal and vertical direction as a function of total porosity fraction:

$$\sigma_c^H = 8[1 - \sqrt{\frac{\nu_T}{0.7}}]^2 \tag{22}$$

$$\sigma_c^v = 24[1 - \sqrt{\frac{\nu_T}{0.7}}]^2 \tag{23}$$

Cantilever ice beams loaded in bending, fail in the top section where the tensile stresses are the largest. By applying the Von Mises criteria, the flexural strength of a cantilever beam with a point load applied at the free end, is the maximum horizontal stress when the ice yields. If the ice is homogeneous and the beam cross section is a rectangle, the horizontal stress has a linear distribution in the vertical direction; $\sigma_f = \frac{M}{I}z$. When the beam is bent down, the part above the neutral axis experiences tension while the part below the neutral axis experiences compression. Beam theory and equations used to express flexural strength in bending are derived in section 2.3. Schulson (1983) observed that for ice; tensile strength was significantly lower than compressive strength. By applying beam theory, it is seen that the tensile stress in the top fibres of the beam is equal to the flexural strength, $\sigma_f(z = \frac{h}{2}) = \sigma_T$.

Flexural strength in ice sheets depends on the physical properties e.g. temperature and porosity. Timco and O'Brien (1993) collected data for flexural strength and porosity of two thousand, four hundred and ninety-five cantilever beam samples. The correlation they found is given in figure 11. Plots of flexural strength σ_f as a function of the brine fraction coincided fairly well with the expression:

$$\sigma_f = 1.76e^{-5.88\sqrt{\nu_b}} \tag{24}$$

Timco and O'Brien (1993) also plotted flexural strength against ice temperature. The temperature affects the ice both through regulating the ice crystal strength and the brine content. Colder ice may have stronger crystals and less brine, and therefore higher strength. Flexural strength is plotted against temperature in figure 12. The sensitivity of the flexural strength to temperature for warm sea ice suggest that the main effect of the temperature is that it changes the brine volume.

Another factor affecting the ice strength is the test machine and apparatus. A mobile test apparatus is used in the field to reduce the time between sampling and testing making the test conditions as close to in-situ as possible. Sinha and Frederking (1979) investigated how test apparatus, through the system stiffness, could affect failure and the elastic modulus in ice.

Stiffness is generally given as:

$$k = E\frac{A}{l}, \tag{25}$$

where E is the elastic modulus, A is the sample cross section area and l is the sample length. Relative system stiffness is the ratio between loading stiffness k_l and sample
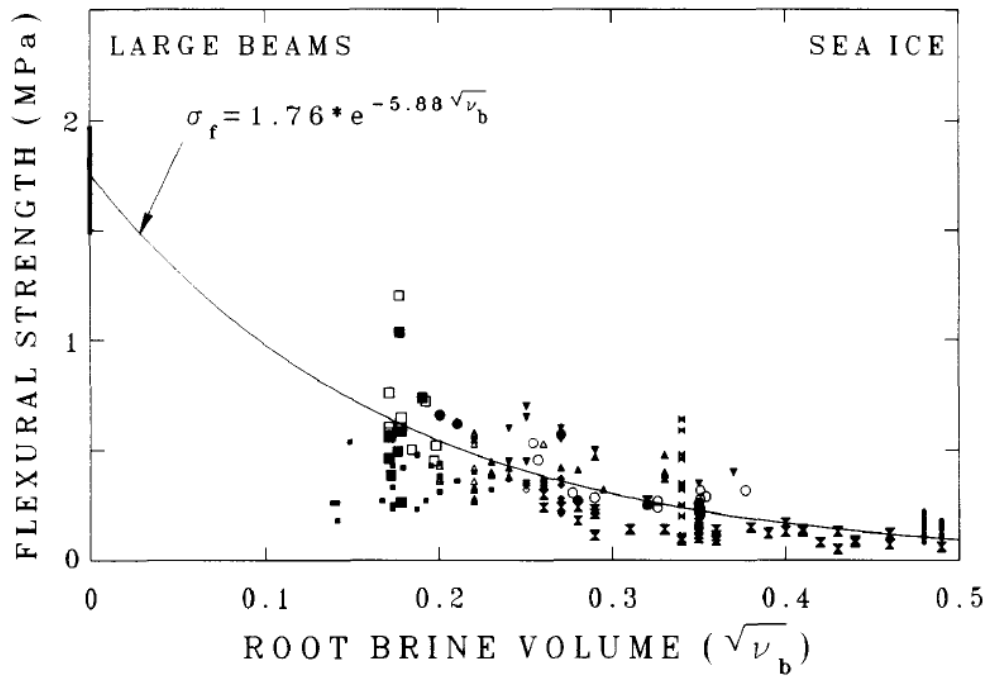
Figure 11: Flexural strength vs. root brine fraction. Timco and O'Brien (1993)
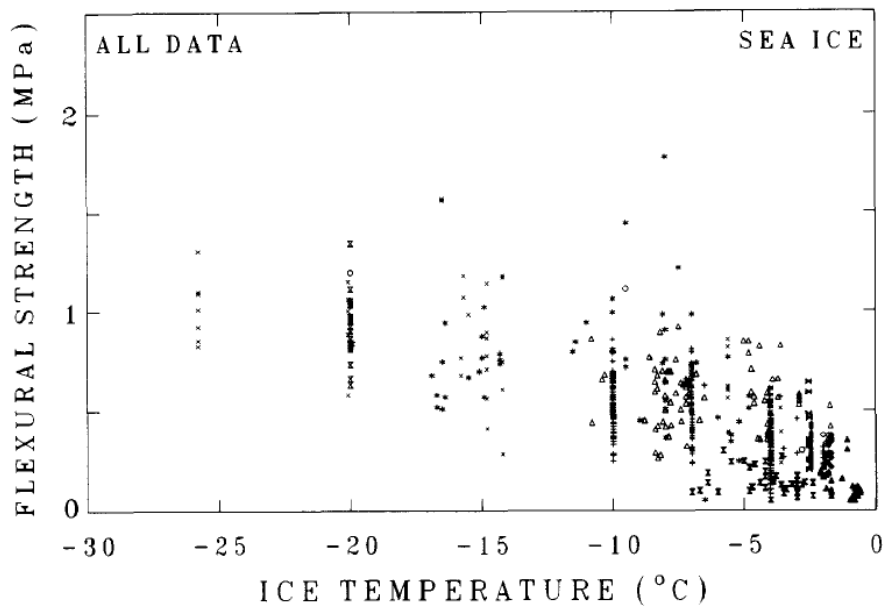
Figure 12: Flexural strength vs. temperature. Timco and O'Brien (1993)

stiffness k_s. Loading stiffness is a parallel summation of test machine stiffness k_m and load spreading accessories (platens etc.) stiffness k_a.

$$k_r = \frac{k_l}{k_s} \tag{26}$$

Sinha and Frederking (1979) observed the following effects of system stiffness:

- Ice strength is a function of relative system stiffness, if results are considered in terms of nominal strain rates. If strength is expressed as a function of stress rate instead, test system influence is greatly reduced.

- Low capacity test machines leads to lower stress rates and consequent lower ice strength.

- Compliant platens, cardboard layers etc. introduces an elastic spring to the system, reducing the relative system stiffness reducing the sample stiffness.

Sinha and Frederking (1979) performed their tests on test rigs with loading capacities of 1.25MN, 0.1MN and 0.2MN. Labelling the 1.25 MN a high capacity machine and the two latter low capacity machines. Mobile test apparatus are often low capacity machines coinciding with ductile-like yield failure. "KOMPIS" the test rig used in tests for this work is a soft machine, with a capacity of 0.095MN.

The total stiffness, when $k_a = 0$ e.g no platens etc., is given by the parallel summation:

$$\frac{1}{k_T} = \frac{1}{k_s} + \frac{1}{k_m} \qquad (27)$$

The total stiffness is the measured stiffness from the compression test. If the machine stiffness is know, it can be used to find a better estimate for the specimen stiffness from equation 27 and 25, namely:

$$E_s = \frac{l}{A}\left(\frac{1}{k_T} - \frac{1}{k_m}\right)^{-1}, \qquad (28)$$

The uni-axial test is used to determine effective modulus as well as strength. Because the system stiffness of a mobile test apparatus reduces the stiffness of the system, the elastic modulus should be taken as the steepest slope of the stress-strain curve. It is coinciding that ice with similar physical properties tested in-situ has lower strength than ice tested in a lab, with stiffer test machines. Therefore it is stressed that it may be incorrect to label values for the Young's modulus and uni-axial strengths, obtained by in-situ tests, true values.

Since strength is associated with failure, something should be said about failure in ice. Fracture is in general controlled by two different processes, namely *nucleation-* and *propagation-* controlled fractures. The different processes leads to either brittle or ductile failure, respectively. Nucleation-controlled failure occur if an applied load nucleates micro-cracks large enough to instantly propagate leading to failure. On the contrary, failure is propagation-controlled when the nucleation of micro-cracks is insufficient to cause failure and further load must be applied to propagate macro-cracks. Sanderson (1988) found that grain size diameter influence the type of failure in ice. For grain size diameters less than 1.5 mm, failure was found to be propagation-controlled and for larger grain sizes nucleation-controlled. He found temperature dependency to lead to minor variations (10-20%). Pre-exciting flaws will

cause strength to be reduced. In the simplest case of rapid loading and linear elastic fracture theory, propagation of flaws is controlled by crack length (2a) according to equation:

$$\sigma = \frac{K_{IC}}{\sqrt{\pi a}},\tag{29}$$

where K_{IC} is the fracture toughness.

A large ice sample is more likely to have more and bigger flaws compared to a smaller sample and because of this strength of ice is expected to show a pronounced scale effect (Sanderson, 1988).

This far materials have been classified as brittle or ductile, there is however a transition between the two, namely quasi-brittle materials. The fracture zone is larger compared to brittle and ductile fracture zones. These materials do not harden, they show a pronounced *softening* behaviour. When load is applied it increases linearly up to the elastic limit upon which it decreases. Stresses are transferred across the crack tip according to a given softening function. The size of the fracture zone is dependent of the softening function. In the case of a linear softening function compared to a ductile perfect plastic- and an brittle elastic material, the fracture zone of a quasi-brittle will be larger than ductile materials that harden or brittle materials, seen in figure 13. Ice may be classified as a quasi-brittle material (Bazant and Planes, 1998), softening parameters for ice should however be comprehensively investigated.
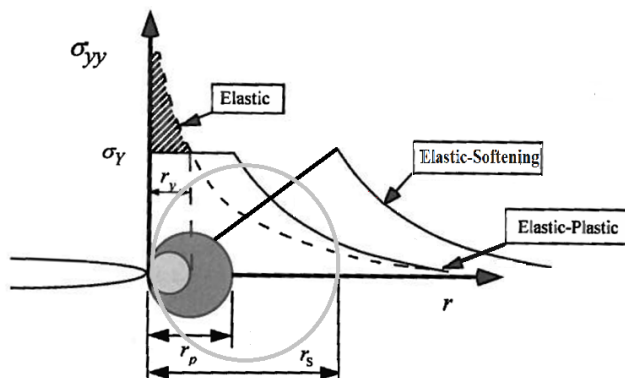
Figure 13: Flexural strength vs. root brine volume. Timco and O'Brien (1993)

2.3   Beam theory

In this section beam equations are derived. A beam is in the most general form a plate that extends only in one direction.

A floating ice cover can be considered a thin plate of thickness h in the z-direction, extending in the horizontal x,y-plane. In figure 14 a general plate with directions and stresses is shown. In this thesis deflection in the z-direction is labelled w, in x-direction u and y-direction v.
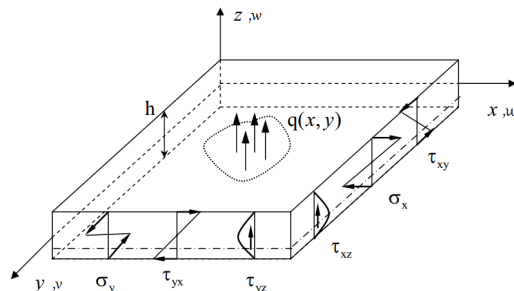
Figure 14: A general plate (Holm, 2010)

Flexural strength is studied by making beams from an ice cover, a beam is a plate where the x dimension, the length, is much greater than the y, the width, and z, the thickness. A general beam with direction and deflection labels used in the thesis, is shown in figure 15.
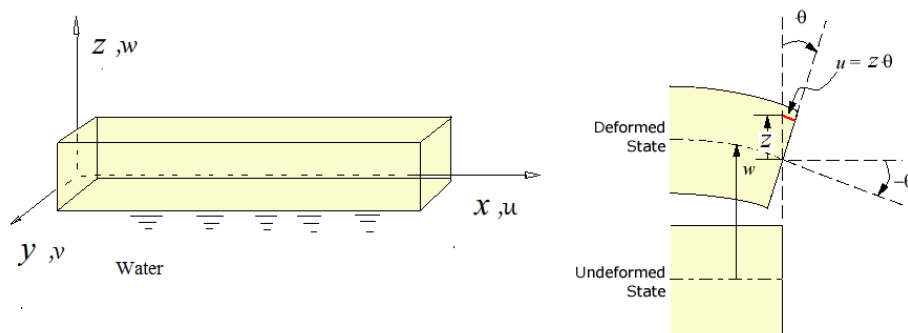
Figure 15: A general cantilever beam.

2.3.1   Standard beam theory

In the proceeding, Euler-Bernoulli beam theory is used to derived a general expression for the stress through the beam in the x-direction. The stress in the x-direction will be used to determine the flexural strength. In this general case the effective modulus is assumed to be a function of the z-direction $E(z)$, more on this assumption in section 2.3.2. The formulas are derived by starting with the plate and the total strain energy equation for all six stresses and strains:

$$U = \frac{1}{2} \int\int\limits_{V}\int (\sigma_x \epsilon_x + \sigma_y \epsilon_y + \sigma_z \epsilon_z + \tau_{xy} \epsilon ex + \tau_{xz} \epsilon_{xz} + \tau_{yz} \epsilon_{yz}) \mathrm{dV} \qquad (30)$$

In the Euler-Bernoulli beam theory, where dimensions $b \ll L$ and $h \ll L$, uni-axial stress in the y and z direction are negligible, so are the shear strains :

$$\sigma_y \ll \sigma_x ; \sigma_z \ll \sigma_x, \qquad (31)$$

$$\epsilon_{xy} = \epsilon_{yz} = \epsilon_{zx} = 0, \qquad (32)$$

The only term left in strain energy equation 30 is the stress and strain in the x-direction.

$$U = \frac{1}{2} \int\int\limits_{V}\int \sigma_x \epsilon_x \mathrm{dV} \qquad (33)$$

Strain in the x-direction ϵ_x is given by the derivative of the displacement in the x direction, u(x,z), with respect to x:

$$\epsilon_x = \frac{\partial u}{\partial x} \qquad (34)$$

Displacement u(x,z) is given by the displacement along the x-direction, lets call it $\hat{u}(x)$, and the displacement from bending u(z), seen in figure 15.

$$u = \hat{u}(x) + z\theta(x) \qquad (35)$$

θ is shown in figure 15, the rotation is assumed to be small hence $\sin(\theta) \simeq \theta$. The rotation θ equals the curvature of the curved beam :

$$\theta = -\frac{\partial w}{\partial x} \qquad (36)$$

In pure bending there is no force acting in the horizontal x-direction and therefore no displacement:

$$\hat{u} \equiv 0 \qquad (37)$$

The resulting displacement, u, is:

$$u = -z\frac{\partial w}{\partial x} \qquad (38)$$

From equation 34, the strain in the x-direction is:

$$\epsilon_x = -z\frac{\partial^2 w}{\partial x^2} \tag{39}$$

By applying Hooke's law and equation 39 the stress σ_x is:

$$\sigma_x = E(z)\epsilon_x = -zE(z)\frac{\partial^2 w}{\partial x^2} \tag{40}$$

The strain energy becomes:

$$U = \frac{1}{2}\int_0^L \int_{-b/2}^{b/2} \int_{-z_0}^{h-z_0} \sigma_x \epsilon_x \mathrm{dzdydx} \tag{41}$$

$$= \frac{1}{2}\int_0^L \int_{-b/2}^{b/2} \int_{-z_0}^{h-z_0} E(z)\epsilon_x^2 \mathrm{dzdydx} \tag{42}$$

$$= \frac{1}{2}\int_0^L \int_{-b/2}^{b/2} \int_{-z_0}^{h-z_0} z^2 E(z)(\frac{\partial w}{\partial x_2})^2 \mathrm{dzdydx} \tag{43}$$

The moment of inertia I_1 is introduced as:

$$I_1 = \int_{-b/2}^{b/2} \int_{-z_0}^{h-z_0} z^2 E(z)\mathrm{dydz} = b \int_{-z_0}^{h-z_0} z^2 E(z)\mathrm{dz} \tag{44}$$

The remaining strain energy is:

$$U = \frac{1}{2}\int_{x_2}^{x_1} I_1(\frac{\partial^2 w}{\partial x_2})^2 \mathrm{dx} \tag{45}$$

The moment in the x-direction is the stress $\sigma(z)$ times the arm z, integrated over the cross section area, then by using the correlations given in equation 40 and equation 44 the moment is expressed as follows:

$$M_x = \int \int_A \sigma_x z \mathrm{dA} = -I_1 \frac{\partial^2 w}{\partial x^2} \tag{46}$$

The neutral axis, namely z_0, is the axis where the stress is zero. By using (40), the neutral axis is found to be:

$$\int_{z_0}^{h-z_0} \sigma_x \mathrm{dz} = \int_{z_0}^{h-z_0} E\epsilon_x \mathrm{dz} = \int_{z_0}^{h-z_0} -zE(z)\frac{\partial w}{\partial x^2}\mathrm{dz} = 0 \tag{47}$$
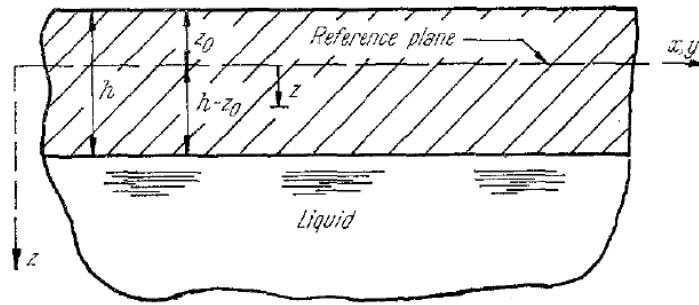
Figure 16: Beam hight and neutral axis (Kerr and Palmer, 1972)

Since $\frac{\partial^2 w}{\partial x^2}$ is independent of z, the following equation determines the neutral axis position:

$$\int\limits_{z_0}^{h-z_0} -zE(z)\mathrm{d}z = 0 \tag{48}$$

By combining equation 46 and 40 the well known stress formula is obtained:

$$\sigma_x = \frac{M_x}{I_1}zE(z) \tag{49}$$

It is stressed that the effective modulus, in formula 49, is a function of the z-direction and not a constant.

2.3.2 Cantilever beam

The cantilever beam test is used to determine the flexural strength of a floating ice sheet. Flexural strength is the loading capacity in bending. As an attempted to measure values for flexural strength in level FY sea ice it has been recommended to perform an in-situ [3] cantilever beam test (Schwarz, 1981). The advantage of this test compared to a three or four point bending test, seen in figure 17, is that the ice remains in its natural environment avoiding brine drainage and maintaining the natural temperature gradient. The flexural strength is an indirect result of the cantilever beam test where the ice is assumed to be homogeneous, isotropic and the loading quasi-static. This is off course a simplification because of the natural variation of properties throughout the ice cover. Traditionally Timco and O'Brien (1993) and Marchenko (2011) makes the above assumptions together with neglecting the water foundation, when finding the flexural strength by equation 51. The test set-ups can be seen in the figure 17.

---

[3]In-situ is a latin phrase that translate into "in position", the cantilever ice beam is kept in its natural environment during the test Kämäräinen (1993).
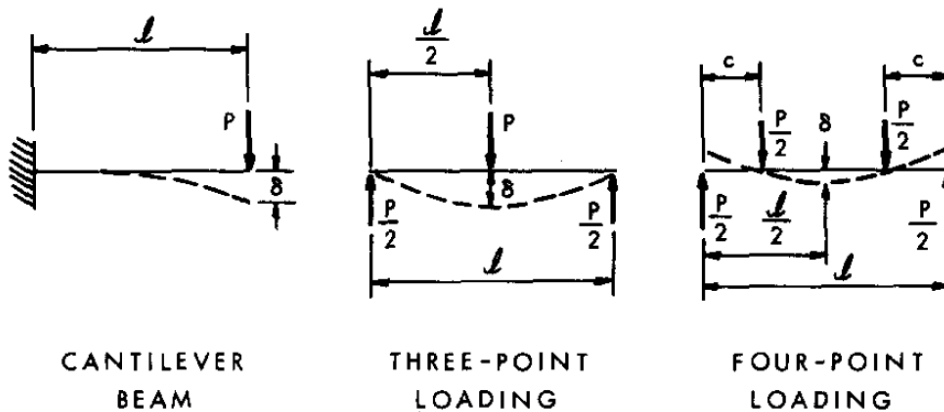
Figure 17: Beam geometry (Schwarz, 1981)

When choosing beam geometry and constructing the test set-up, certain precautions should be taken. Schwarz (1981) recommends that the beam length should be 7-10 times the ice thickness and that the width is 1-2 times the ice thickness or at least 10 times the crystal diameter. A shorter beam could lead to shear failure whereas a wider beam can result in biaxial effects requiring plate theory. During the field work in Svea three shorter beams where loaded to investigate if decreasing the length of the beam would lead to shear failure. A detailed study of the effects of beam geometry is found in (Hirayama, 1990), here a summary is given:

- no difference in flexural strength found for a length thickness ratio of $2.5 < L/h < 11$

- no difference in flexural strength found for a width thickness ratio of $0.5 < b/h < 2.3$

- no difference in flexural strength found for a length width ratio of $2 < L/b < 17$

- no difference in flexural strength found for a width crystal diameter ratio of $b/d > 15$

Further when cutting out the beam, a radius of cut should be made at the root of the beam to avoid stress concentrations that may reduce the flexural strength index, it has been recommended that this radius should be 1/15 of the beam width. It seems that the importance of stress concentration effects increases with increased brittleness (Schwarz, 1981).

Loading rate should also be considered, although it is seen that tensile strength is less dependent on loading rate than compressive strength, according to figure 10, flexural strength is influenced by extreme loading rates. At very low loading rates viscous effects dominate, at higher rates inertia effects of the beam and the displaced water come in to play and for very high loading rates waves are generated and shear becomes significant. Schwarz (1981) recommends, for a typical beam geometry, that a loading time of one second yields satisfactory results .

Assuming an isotropic homogeneous elastic material with a constant stiffness and applying beam theory derived in section 2.3, the flexural strength is found from the following:

$$\sigma = \frac{M}{I_z} z \tag{50}$$

The largest moment is found at the root of the beam, $M = FL$, the corresponding stress in tension is located at the upper part of the cross section, if the material is considers homogeneous the neutral axis , being the x-axis where $\int\limits_{z_0}^{h-z_0} \sigma_{xx} \mathrm{d}z = 0$, coincide with the middle plane $z = \frac{h}{2}$. I_z is the moment of inertia, and for a rectangular cross section area $I_z = \frac{bh^3}{12}$. This gives the following formula for the flexural strength:

$$\sigma(0) = \frac{6FL}{bh^2} \tag{51}$$

The free end deflection is found from the same theory and is given by the formula Cook and Young (1999):

$$w(L) = \frac{FL^3}{3EI} \tag{52}$$

If the ice is in-homogeneous and an-isotropic in the z-direction, then the stress is found from equation 49 and I 44:

$$\sigma(0) = \frac{FLz_0}{I_1} E_{top}, \tag{53}$$

free end deflection:

$$w(L) = \frac{FL^3}{3I_1} \tag{54}$$

2.3.3   Beams with Winkler foundation

In the previous, the moment has been taken to be linear only considering the point load at the free end. A question that should be evaluated is whether the water foundation should be included, resulting in a non-linear distribution of moments in the beam. In an attempt to describe the ice-water interaction a Winkler foundation will later be reviewed and a numerical analysis will be performed, in order to determine the significance of the water.

The Winkler foundation is an elastic foundation that was originally used when describing the deflection occurring on railway rails. Railways are not rigid as they rest on soil and deform by passing trains. A Winkler foundation will in this thesis be

used to describe the water supporting the ice. According to Cook and Young (1999) a Winkler foundation will be exact when a prismatic beam is floating on a liquid without any submerged parts. As is the case for the ice.

The Winkler foundation consists of a number of linear springs with a stiffness K_0. The load from the foundation is proportional to the vertical displacement $w(x)$. The load is given $F(x) = K_0 w(x)$

There are certain limitations to the Winkler foundation, these are:

- It resists only forces normal to its surface

- Contact is never broken between the beam and the foundation

- Deflection of the material represented by the elastic foundation occurs only where the foundation is loaded, as shown in 18 (b).

The beam studied in this thesis is only loaded in the vertical direction, normal to the surface. A' priori to failure contact between the foundation and the beam will not be broken because the load is oriented downwards. Objects floating in water will in general be submerges, with water surrounding the object as shown in figure 18 (b), the assumptions summaries here are shown in figure 18 (b) and are assumed to coincide well with how water acts on a floating beam.
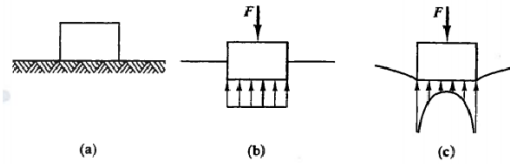
Figure 18: Block on elastic foundation. (a) no load applied (b) load applied no deflection of water(c) solid elastic foundation, with deflection of water Page 134 in Cook and Young (1999)

The formulas for the maximum deflection and stress are all derived in Appendix.

The momentum at the fixed end is given:

$$M(0) = \frac{F}{\beta} \frac{\sinh \beta L \cos \beta L + \cosh \beta L \sin \beta L}{\cosh^2 \beta L + \cos^2 \beta L} \tag{55}$$

Where beta β is an expression, if the ice in considered homogeneous and isotropic then β is given:

$$\beta = \sqrt[4]{\frac{k}{4EI}} \tag{56}$$

Stress in at the crack root is:

$$\sigma(x=0) = \frac{6}{bh^2} \frac{F}{\beta} \frac{\sinh \beta L \cos \beta L + \cosh \beta L \sin \beta L}{\cosh^2 \beta L + \cos^2 \beta L} \tag{57}$$

Corresponding to the deflection of the free end:

$$w(L) = \frac{2F\beta}{k} \frac{\sinh 2\beta L - \sin 2\beta L}{\cosh^2 \beta L + \cos^2 \beta L} \tag{58}$$

If however the ice is considered in-homogeneous and an-isotropic in the z-direction then β_1 is expressed though I_1 and equation 49.

$$\beta_1 = \sqrt[4]{\frac{k}{4I_1}} \tag{59}$$

The moment is also expressed according to β_1, as:

$$M(0) = \frac{F}{\beta_1} \frac{\sinh \beta_1 L \cos \beta_1 L + \cosh \beta_1 L \sin \beta_1 L}{\cosh^2 \beta_1 L + \cos^2 \beta_1 L} \tag{60}$$

Stress at the root crack is:

$$\sigma(x=0) = \frac{z_0 E_{top}}{I_1} \frac{F}{\beta_1} \frac{\sinh \beta_1 L \cos \beta_1 L + \cosh \beta_1 L \sin \beta_1 L}{\cosh^2 \beta_1 L + \cos^2 \beta_1 L} \tag{61}$$

The deflection on the free end is given as:

$$w(L) = \frac{2F\beta_1}{k} \frac{\sinh 2\beta_1 L - \sin 2\beta_1 L}{\cosh^2 \beta_1 L + \cos^2 \beta_1 L} \tag{62}$$

2.3.4 Varying elastic modulus E(z)

It was shown in section 2.1.3 that physical properties varied through the ice thickness, especially when air temperatures were cold. In this section a variation of elastic modulus across the ice thickness is described.

Kerr and Palmer (1972) published an article on flexural strength with spatial variation of the elastic modulus throughout the ice thickness $E(z)$. A review of this paper showed that a varying elastic modulus across the ice thickness strongly affected the stress distribution. Kerr and Palmer (1972) used an exponential function for the distribution for the elastic modulus across the ice thickness (equation 63).

$$E = E_0[1 - (1 - \alpha)(\frac{z}{h} + \frac{z_0}{h})^n], \tag{63}$$

where E_0 is the elastic modulus of the top fibres, h is the ice thickness, z_0 is the neutral axis given in figure 16 and α and n are curve fitting parameters. With this

equation (63) for the elastic modulus, the neutral axis can be found according to equation 47, and is:

$$z_0 = h\frac{(n + 2\alpha)(n + 1)}{2(n + 2)(n + \alpha)} \tag{64}$$

The authors of this paper mention little of how they found the expression for the elastic modulus, and why or when it would be applicable for expressing the elastic modulus-distribution across the ice thickness.

A small not on the y-direction dependency should be made; the elastic modulus is taken as a function of the z-direction only. For the cantilever beam test there is additionally a y-direction dependency. During the dark season when air temperatures are low, the warm water surrounding the beam when it is cut free, may influenced the cold top layer of the ice. In this sense the elastic modulus would be a function of both y and z ($E(z, y)$). This can however be neglected by keeping the beam dry as long as possible before the test is performed (Kerr and Palmer, 1972).

3 Site and experimental set-up

Contents

Experimental work has been a key aspect of this thesis, a significant work was put into preparations for these tests. In order to study how flexural strength depends on spatial variations through the ice thickness and physical ice properties, two scientific expeditions on sea ice were designed and executed. The first expedition was performed in Svea bay in Van Mijenfjorden on Svalbard, between the 05th and 16th of March 2013.

The second expedition was performed on the research vessel "Lance RV" during an expedition in the Barents sea to the south east of Edgeøya in spring, between the 25th of April and 04th of May 2013. Six cantilever beam tests, temperature, salinity, porosity and uni-axial compression tests were performed on each expedition.

3.1 Svea bay in Van Mijenfjorden on Svalbard

Van Mijenfjorden is situated on the west coast of the island Spitsbergen, in the Svalbard archipelago in the north-western Barents sea about 60 km from Longyearbyen, it reaches about 70 km long. The island Akseløya nearly blocks the mouth of the fjord offering favourable ice conditions. The fjord is often divided into an outer and inner basin (Høyland (2009)). We performed our measurements in the inner basin of Van Mijenfjorden marked on the map in figure 19. A camp was made at this position. All experiments were executed in a radius of about 20 m from the camp site located south of Barrynestet. Ice thickness and approximate water depth was measured at 4 different locations before the final camp site was chosen. The ice thickness ranged between 63-68 cm, and the water was shallow at two of the positions closest to shore. We chose to make the camp at a site where the ice thickness was 63 cm and the water was relatively deep, to avoid coastal ice according to section 2.1.3. Temperature data from the site is shown in figure 20, temperatures measured on site reached -32.3 measured the 07th of March, the low temperatures was challenging for electronic equipment as well as safe operations.
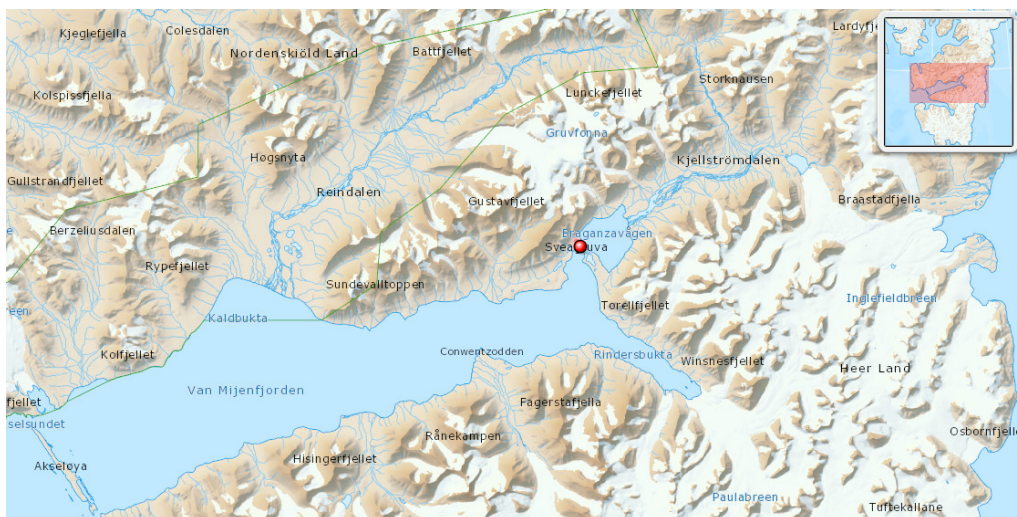
Figure 19: Map of Van Mijenfjorden in Svea bay on the west coast of Spitsbergen. The tests were performed in the inner basin of the fjord marked on the map. (http://toposvalbard.npolar.no)
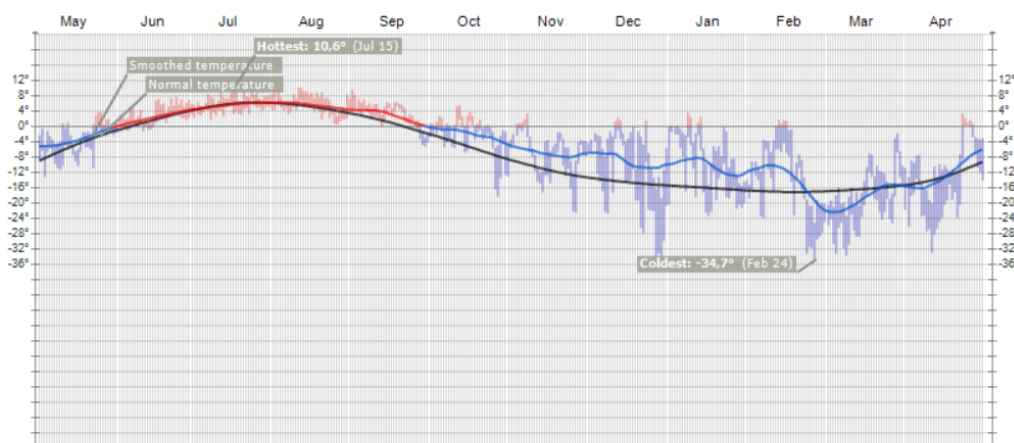
Figure 20: Temperature statistics. (http://yr.no)

3.2   The Barents sea south east of Svalbard

Two different sites near Edgeøya on the south-east coast of the Svalbard archipelago were used to test sea ice properties of ice in the north west Barents sea, in spring. In order to get to level ice "Lance RV" followed the tracks of the coastguard ship "KV Svalbard " with the DNV- classification "icebreaker polar 10". Level ice thickness at the first site was measured to be approximately 40 cm with surface water, we reached the ice sheet on the evening 27th of April and stayed there until the evening 28th. Level ice thickness at the second site was measured to be approximately 50-60 cm with some surface water, at both locations there were several ice ridges surrounding the ice floes. We stayed at the second position 29th and 30th of April. Air temperature during the expedition was around $-3°$ with mostly calm and clear weather.
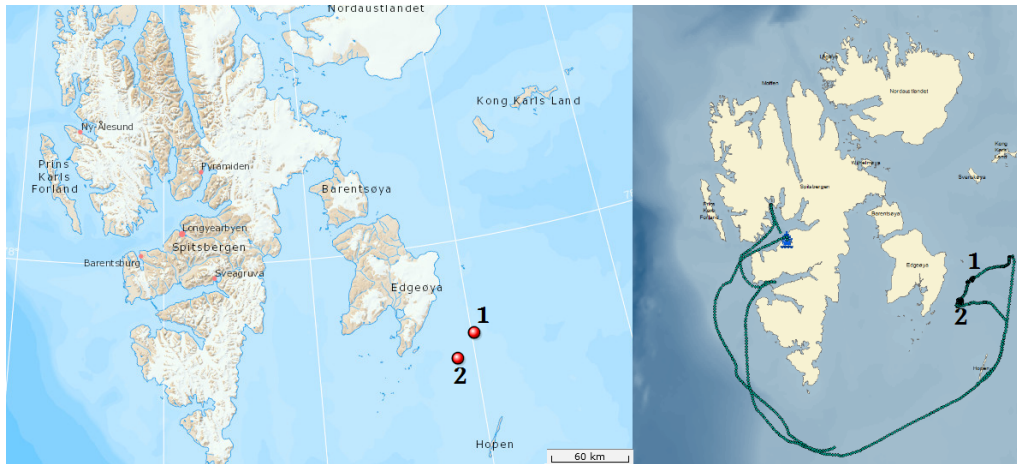
Figure 21: Map of the two test sites on the south east coast of the Svalbard archipelago. (http://toposvalbard.npolar.no) GPS-track of Lances path.
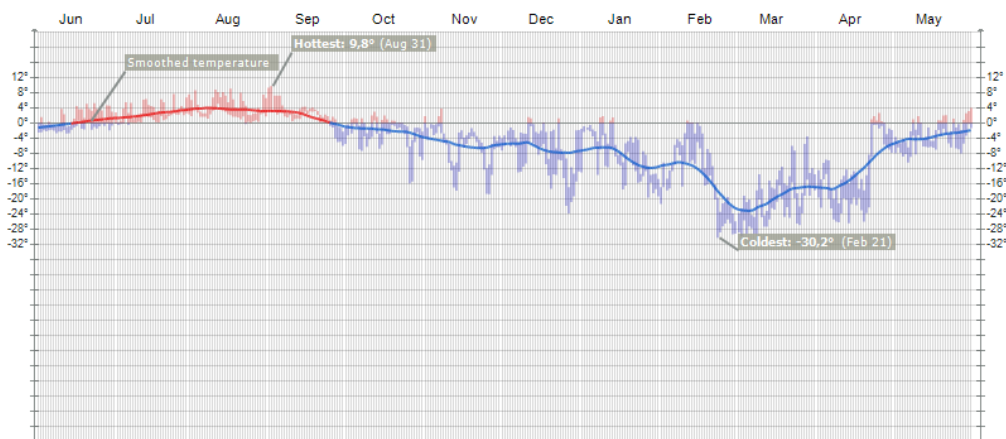
Figure 22: Temperature statistics Edgeøya. (http://yr.no)

3.3   Set up for ice properties

In this section the test set up for physical property measurements, as well as the uni-axial compression tests will be presented. Both physical and mechanical properties were measured on site, with an exception of thin sections which were done in the cold lab at the university centre in Svalbard (UNIS) the 16th of May.

3.3.1   Set up for physical properties

Physical properties measured on site were; ice and snow thickness, temperature, salinity and density. Additionally core samples were collected from both expeditions in order to study grain structure, by thin sectioning. Salinity and temperature were measured from vertical ice cores taken with a Kovacs drill. Temperature cores had a diameter of 70 mm with lengths ranging from 40 mm up to 70 mm. Ice temperature was measured by drilling holes in the sample to fit a digital thermometer in. Temperature was measured at every 50 mm of the core sample, starting from

the bottom. We made several attempts to measure density, for porosity calculations, samples often broke when we took them out of the Kovacs drill so that the cylinder length became uneven and volume measurements inaccurate. Ice thickness was measured by drilling holes and using a measuring rod with a hook in one end, which we attached to the ice bottom.

Thin sections of samples were made to study the grain size and structure of the ice. Thin sectioning must be performed in a cold lab with temperatures preferably below -20 °. An approximate 1 cm section of the ice is cut out with a band saw and glued to two glass plates with water. This ice section is further divided into two sections with the band saw and planed with a micrometer cutter. Thin sections are studied in a polarisation lens to see grain boundaries clearly. The process of making a horizontal thin section is shown in figure 23.

When glueing the ice to the glass plates it is important to prevent water from creeping in between the glass plate and the ice, this forms an ice layer distorting the image of the sea ice grains. Additionally, the micrometer cutter should be used with care so that the ice does not fracture.
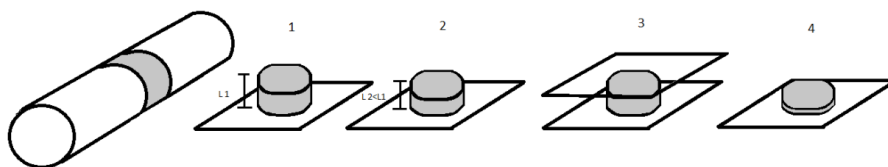
Figure 23: The process of making a horizontal thin section (Ervik Åse (2012)).

3.3.2   Set up for uni-axial compression tests

Both horizontal and vertical uni-axial compression tests were performed and planned. Samples were taken out with a Kovacs drill. We used the test machine "KOMPIS" (1) in figure 24, a test rig developed by M-tech in Trondheim (Moslet (2007)), connected to a data-logger called "SOFTIS" (2) this was again collected to a computer where data files with load and displacement were stored. Data points were sampled every 0.1 seconds, the nominal strain rate was 10^{-3} for all compression tests. The real strain rate was found by Moslet (2007), he estimated it to be 7×10^{-4} and the loading capacity was 0.095 MN with a stiffness of 0.2 GN/m i.e. a soft test machine (see section 2.2).

In order to collect horizontal samples blocks of ice were cut and lifted out of the water. In the bay of Svea temperature gradients were large and measurements were therefore began on the warm bottom part of the ice. In Svea, it took approximately 10 minutes from a block was lifted until drilling started, it took in total 5-10 minutes between each core sample was compressed. All samples were sawn by "DISCOS" and had a diameter of 70 mm and length of about 175 mm (dimensions were additionally measured). Ice cores were compressed until the load peaked. Uni-axial compression

tests were used to determined effective modulus and compressive strength at different depths of the ice in both horizontal and vertical direction. The horizontal samples were used to determine the distribution of $E(z)$, dimensions of these samples are given in table 1.

Table 1: Data for ice core samples used in uniaxial compressive tests, Svea bay.

Label	Location	Direction*	Diameter [mm]	Length [mm]	Depth** [mm]	Distance***
S1	C1****	v	70	173	45	-
S2	C1	v	70	170	293	-
S3	C1	v	70	170	478	-
S4	C1	v	70	170	0	-
S5	C1	v	70	170	188	-
S6	C1	v	70	160	463	-
S7	Cs3	h	70	170	505	15
S8	Cs3	h	70	170	505	220
S9	Cs3	h	70	175	505	390
S10	Cs3	h	70	175	283	10
S11	Cs3	h	70	170	283	200
S12	Cs3	h	70	169	283	390
S13	Cs3	h	70	170	100	0
S14	Cs3	h	70	170	100	260
S15	Cs3	h	70	170	100	430

v= vertical, h= horizontal. **For S1-S6 vertical depth was measured from the ice cover surface to the upper surface of the ice core, for S7-S15 depth was measured from the ice cover surface to the origin of the core. *** For S7-S15 the horizontal distance was measure from the crack surface of Cs3 to the free end. **** See table 2 for beam labels, S1-S6 were taken from the root of C1.
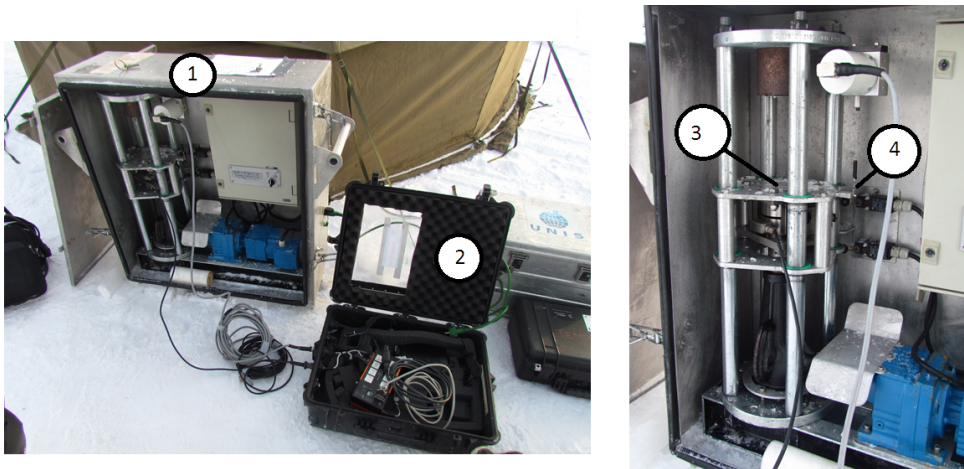
Figure 24: (1)"Kompis" connected to the data-logger (2)"softis". (3) is the plate compressing the sample and (4) is the displacement sensor.

3.4   Beam test set-up

Six cantilever beam tests were designed and executed on each expedition. Prior to all beam tests, beams had to be cut free from the ice cover. Staring by first drawing the geometry in the snow, at a wanted test location, where there was as little snow as possible. No surface water was found in Svea influencing the choice of site. On the Lance-expedition this however determined where to locate the beams. In Svea the snow layer was wind packed, snow depth ranged from 4-8 cm on the chosen locations. Beam dimensions are given in table 2 and 3. To make sure beams were not restrained by the surrounding ice, a 10-15 cm slot of ice was removed around the beams. At the beam root, in each slot, a radius of cut was made with the Kovacs drill having a diameter around 80 mm. Ice thickness determined the beam length and width, following the recommendations given i section 2.3.2. Additionally, beam width was restrained to be less than 70-75 cm by the load cell rig, which was placed over the beam on the ice cover. The various phases of preparation can be seen in figure 25.

Table 2: Beam dimensions from the bay of Svea.

Beam geometry	Label	Length [m]	Width [mm]	Date
Cantilever beam	C1	3,5	0,7	07.03.2013
	C2	3,5	0,7	13.03.2013
	C3	3,5	0,7	13.03.2013
Short cantilever beam	Cs1	1,5	0,7	10.03.2013
	Cs2	0,7	0,7	11.03.2013
	Cs3	0,7	0,7	12.03.2013

Ice thickness was assumed to be in the range 0,65-0,75 m, ice thickness is given in table 10 together with final dimensions.

Table 3: Beam dimensions from the Lance-expedtion.

Location	Label	Length [m]	Width [mm]	Date
1	B1	2.5	0.50	27.-28.04.2013
1	B2	1.5	0.50	28.04.2013
1	B3	2.0	0.45	28.04.2013
2	B4	2.0	0.50	28.04.2013
2	B5	3.0	0.60	29.04.2013
2	B6	3.0	0.60	29.04.2013
2	B7	3.0	0.60	29.04.2013

Ice thickness was assumed to be in the range 0,35-0,60 m, ice thickness is given in table 14 together with final dimensions.

The final dimensions often differed from those first measured, final dimensions can be found in the result section 4.2. After drawing beam geometries chain saws were used to remove ice from the slots, slots were kept dry as long as possible by initially

removing 40-50 cm of ice (in Svea). The last layer of ice was removed by drilling holes approximately 20 cm apart and by using handsaws to remove the last ice. After making the first hole, water filled the slots and rubber gloves were used to remove slush to prevent refreezing. Snow was kept on the beams except from beam Cs2, where the snow was removed. On the south east coast of Edgeøya in the Barents sea, beams could be cut free with chain saws alone. In the Barents sea slots filled with water even when only the first 20 cm of ice was removed.

The loading and measuring rig used in beam testing, shown in Figure 26, consists of a welded steel frame (1) fastened to the ice with chains and turnbuckles (2a). If higher loads are to be expected, additional chains (2b) were used. The beam was loaded using a vertical hydraulic cylinder (3) powered by a generator-driven compressor, load was measured by a load cell (4) placed on the beam under the cylinder. In addition, the displacement of the beam at the loading point was measured with a spring sensor (5a) and a resistance (5b) sensor. Additional sensors, such as an acoustic sensor (6) was also utilized. As seen in Figure 26, the maximum width of the beam was largely limited by the size of the rig. The data-logger has a sampling frequency of 50 Hz, the displacement sensor had an accuracy of 5×10^{-5}m and recorded displacements up to 0.07 m.

Figure 25: Various phases of preparing the beams
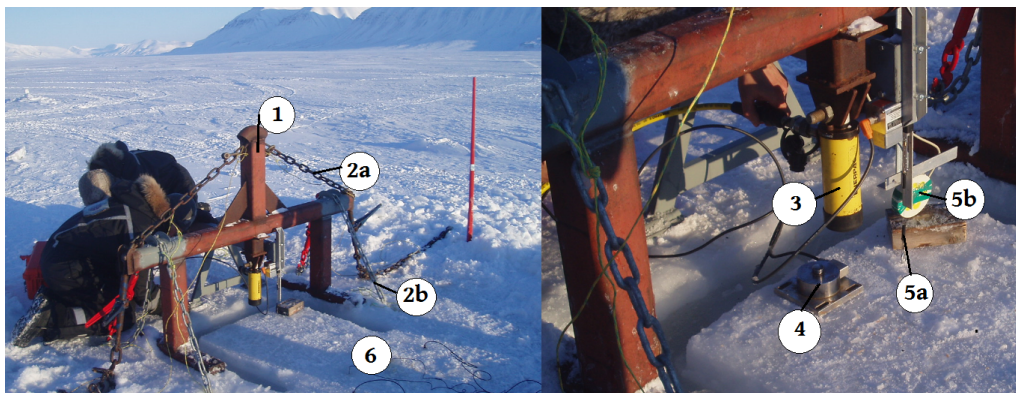
Figure 26: Main beam components, see description

4 Results

Contents

In this thesis data from 3 cantilever beam tests and 3 short cantilever beam tests, together with physical and mechanical property tests will be presented from the sea ice tests in the Van Mijenfjord in Svea bay. Tests in Svea were performed mainly as part of a joint scientific expedition, with professors, PhD students and master students studying mechanical behaviour of sea ice. Additionally a group of students participated from the 12th - 14th of March as part of a field work for the course AT-211 at the university centre of Svalbard, spring 2013. Mechanical and physical property results given in table 4 and 8 as well as figure 34 and35 are based on measurements performed by students, supervised by PhD student Torodd Nord. All other results, except beam C2 and C3, were performed together with the SMIDA group. The author took part as a master student and additionally supervised a group of students performing beam tests C2 and C3.

On the Lance-expedition to the east coast of Edgeøya in the Barents sea, seven cantilever beam tests, together with mechanical and physical tests were measured. This expedition took place as a field work for the course AT-211 at the university centre of Svalbard, spring 2013. I took part as a supervisor for a group of students performing beam tests B1-B7. Mechanical and physical property tests used in this thesis were performed by another group, supervised by Jomar Finseth (adjunct professor, UNIS).

4.1 Ice properties

4.1.1 Physical ice properties

One aim of this thesis is to study how flexural strength relates to physical ice properties. We present here experimental results for properties measured on the same sites as where the beam tests were performed. Temperature and salinity profiles measured in Svea were taken close to the crack root of cantilever beams, dates and beam labels are given in figure 27 and 28.

Temperature and salinity profiles taken from the ice floes in the Barents sea were taken close to beams. Representative profiles are shown in figure 29 and 30.

Grain size of core samples collected in Svea and on Lance is shown on the next page. In Svea horizontal ice cores were taken by students participation in the course AT-307F from the test site a week after the beam tests were carried out. Sections
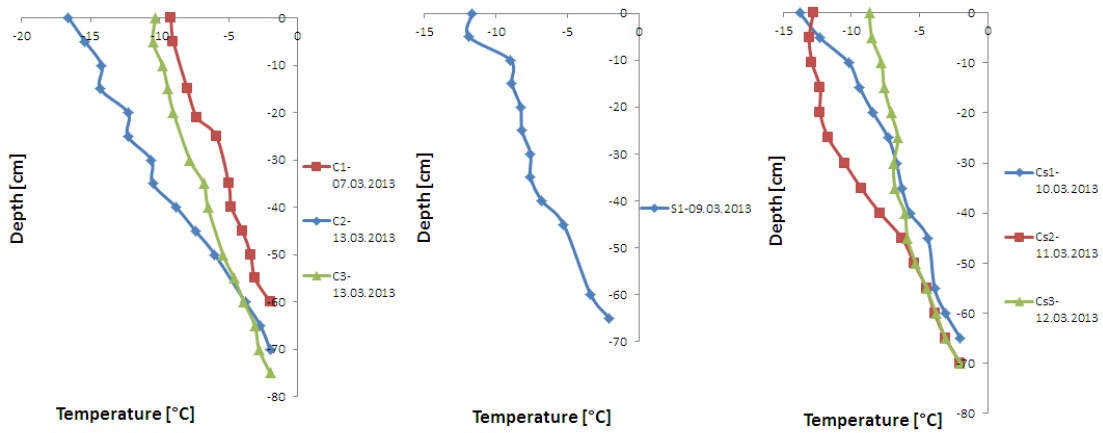
Figure 27: Temperature distribution of ice samples from Svea bay.
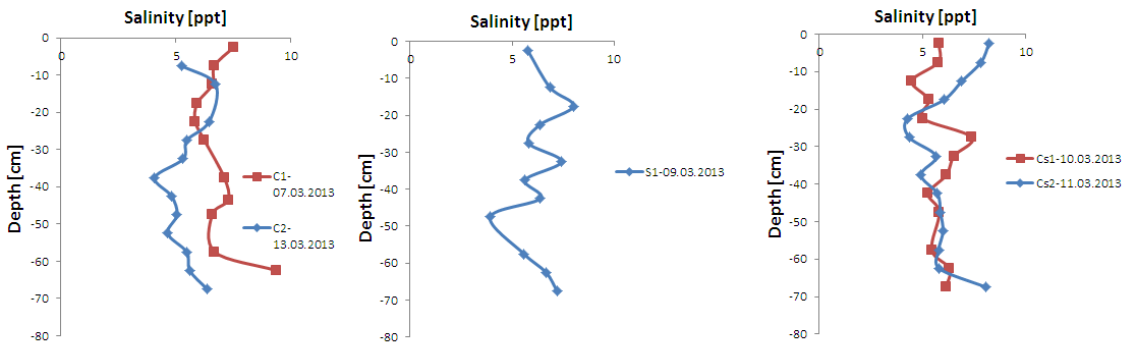
Figure 28: Salinity distribution of ice samples from Svea bay, according to table 4.

shown in figure 31 and 33 were taken at a depth of 30 cm, dimensions of the vertical section is ⌀7 cm, the horizontal section is 7×6 cm.

On Lance, vertical cores were taken at the first site on the 28th of April. A thin section from Lance is shown in figure 32. The core was taken at a depth of 14 cm with dimensions of horizontal section equal ⌀7 cm and vertical section equal 7×9 cm.
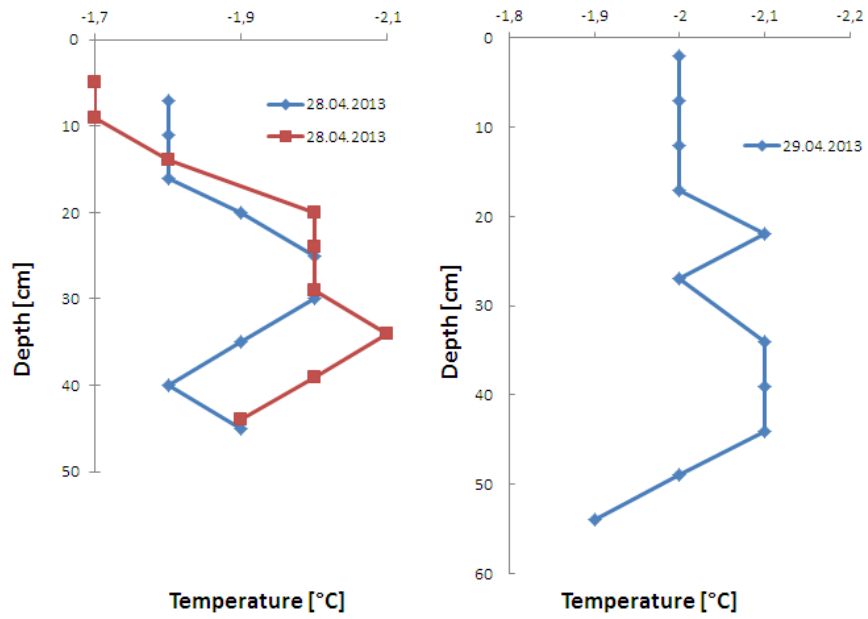
Figure 29: Temperature distribution of ice samples taken during the Lance-expedition, in the Barents sea.
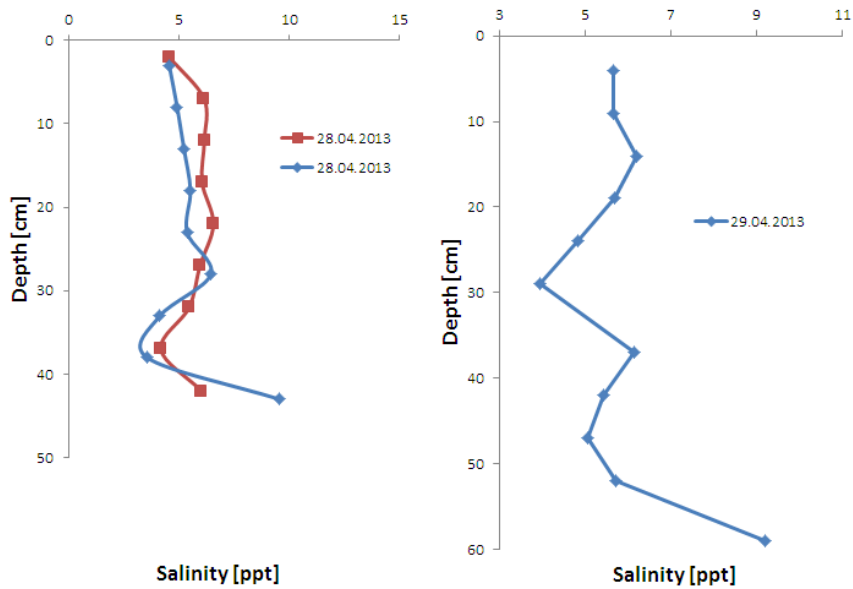
Figure 30: Salinity distribution of ice samples taken during the Lance- expedition, in the Barents sea.
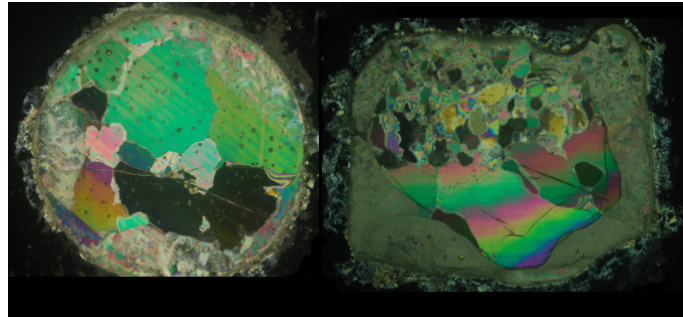
Figure 31: Thin sections of ice taken from Svea bay at a depth of 30 cm. Vertical section with diameter 7 cm. Horizontal section with length of 7×6 cm.
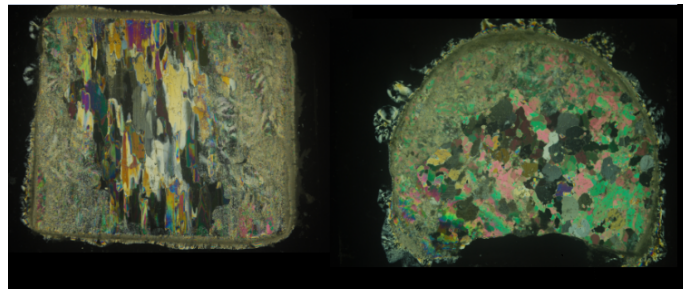
Figure 32: Thin sections of ice taken from the Barents sea at the first location, at a depth of 14 cm. Horizontal section with diameter 7 cm. Vertical section with length of 7×9 cm.
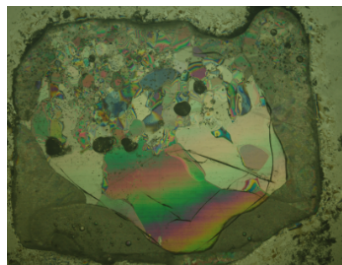
Figure 33: Brine pockets are seen as dark spots, for the horizontal section taken in Svea bay.

Comparison of physical properties of the ice found mid-winter in Svea bay and late spring in the Barents sea. The effect of temperature on brine fraction and compressive strength is shown.
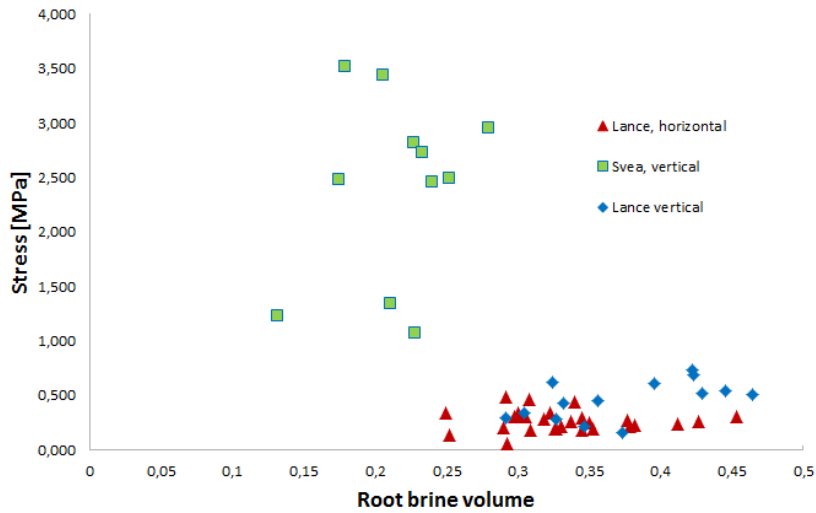
Figure 34: Comparison of the influence of root brine volume on compressive strength from vertical and horizontal samples in Svea bay and the Lance-expedition.
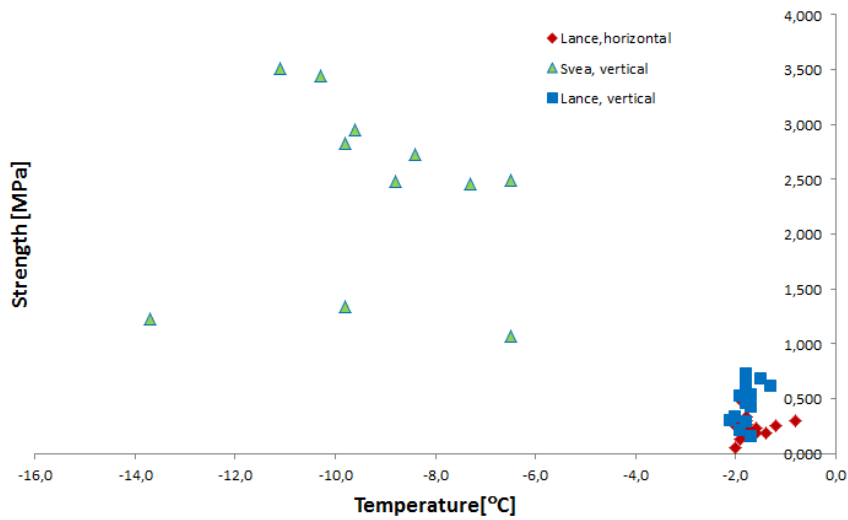
Figure 35: The influence of temperature on compressive strength from vertical and horizontal samples in Svea bay and the Lance-expedition.

Table 4: Ice properties of compression test samples, Svea

Sample	ρ [g/cm^3]	Temp [$^\circ C$]	Sal [‰]	Porosity [‰]	Brine [‰]	Direction	Depth [cm]
Sv1	0.892	-10.3	8.08	80.6	42.3	vertical	37.5
Sv2	0.896	-7.3	8.29	92.5	57.5	vertical	30
Sv3	0.910	-6.5	6.68	70	51.9	vertical	uncertain
Sv4	0.910	-9.8	9.31	72.1	51.7	vertical	30
Sv5	0.851	-11.1	6.8	113.1	32.1	vertical	30
Sv6	0.899	-9.6	13.99	115.9	78	vertical	30
Sv7	0.896	-13.7	4.07	46.7	17.3	vertical	30
Sv8	0.871	-9.8	8.37	105.8	44.5	vertical	35
Sv9	0.825	-6.5	9.02	176.4	63.5	vertical	27
Sv10	0.878	-8.4	7.52	109.5	54.6	vertical	30
Sv11	0.840	-8.8	5.47	122.1	30.5	vertical	30
Sv12	0.754	-13.8	6.35	207.9	22.6	vertical	0

Table 5: Ice properties of compression test samples, Lance. Upper part: horizontal samples. Lower part: vertical samples. L1-L6 and L39-L42 were measured at site 1, L7-L38 at site 2.

Sample	ρ $[g/cm^3]$	Temp $[°C]$	Sal $[‰]$	Porosity $[‰]$	Brine $[‰]$	Depth $[cm]$
L1	0.924	-1.9	5.52	143.4	95.1	37
L2	0.955	-1.8	3.36	95.1	84.9	25
L3	0.940	-1.9	3.21	84.9	115.5	25
L4	0.955	-1.8	4.08	115.5	85.8	36
L5	0.801	-2.0	4.04	85.8	90	26
L6	0.940	-1.8	3.23	90	88.8	36
L7	0.926	-1.9	3.41	88.8	122.5	20
L8	0.948	-1.8	4.36	122.5	118.9	41
L9	0.970	-1.9	4.36	118.9	95.3	24
L10	0.888	-1.8	3.62	95.3	119.2	15
L11	0.962	-1.8	4.18	119.2	90.4	39
L12	0.955	-2.0	3.57	90.4	106.5	26
L13	0.901	-1.6	3.55	106.5	142	13
L14	0.970	-1.8	4.94	142	62.4	39
L15	0.926	-2.0	2.54	62.4	63.8	30
L16	0.859	-1.9	2.64	63.8	113.7	16
L17	0.948	-2.0	4.52	113.7	93.5	39
L18	0.933	-1.8	3.38	93.5	169.8	25
L19	0.970	-1.6	5.25	169.8	109.3	49
L20	0.874	-1.8	4.22	109.3	101.2	34
L21	0.918	-1.9	3.92	101.2	84.3	43
L22	0.911	-1.8	3.12	84.3	145.9	24
L23	0.970	-1.9	5.35	145.9	205.6	49
L24	0.890	-0.8	3.46	205.6	104.3	22
L25	0.933	-1.8	3.77	104.3	106.9	22
L26	0.948	-1.9	4.01	106.9	182.3	15
L27	0.940	-1.2	4.37	182.3	124.7	45
L28	0.896	-1.4	3.65	124.7	92.9	36
L29	0.896	-2.0	3.91	92.9	198.7	32
L30	0.963	-1.7	6.58	198.7	156.7	36.5
L31	0.940	-1.3	4.07	156.7	127	21
L32	0.963	-1.8	4.45	127	184.6	10
L33	0.978	-1.9	6.71	184.6	178.6	33,5
L34	0.978	-1.8	6.16	178.6	105.5	22.5
L35	0.970	-1.8	3.67	105.5	215.4	0
L36	0.955	-1.8	7.61	215.4	120.5	27
L37	0.978	-1.9	4.38	120.5	179.1	34,5
L38	0.963	-1.5	5.24	179.1	85.3	22,5
L39	0.978	-2.1	3.46	85.3	110.2	20
L40	0.955	-1.7	3.68	110.2	139.6	33
L41	0.933	-1.7	4.77	139.6	106.8	0
L42	0.933	-1.8	3.86	106.8	42.3	0

4.1.2   Uni-axial compression results

Uni-axial compression tests were performed in order to determine the elastic modulus and strength of various ice samples. The samples were taken at different depths, in order to study the variation throughout the ice thickness. Samples from a given depth were subjected to uni-axial loads in either of the horizontal and vertical direction, in order to study the possible anisotropy of the elastic properties.

By applying the parallel summation of the stiffness' the total elastic modulus (E_T) can be compared to the samples elastic modulus (E_S). The test machine stiffness was found by Moslet (2007) to be $k = 0,2 GN/m$ at a nominal strain rate of $10^{-3}[s^{-1}]$, $k = E \cdot A/l$. The total elastic modulus and the sample elastic modulus are compared in table 9. In all other tables E is the total elastic modulus found directly from the stress-strain curve.

Mechanical properties of the ice samples collected in Svea bay on the 12th of March 2013, are given in table 7.

Table 7: Ice properties of compression test samples, Svea

Sample	Time to failure [s]	E [MPa]	σ_C [MPa]
Sv1	12.2	700	3.443
Sv2	13.3	578	2.454
Sv3	10.0	299	1.075
Sv4	12.5	685	2.824
Sv5	13.8	598	3.516
Sv6	16.0	830	2.953
Sv7	14.5	*	1.228
Sv8	17.2	*	1.341
Sv9	15.5	309	2.492
Sv10	15.4	729	2.73
Sv11	13.0	614	2.479
Sv12	27.2	21	0.503

* not elastic behaviour
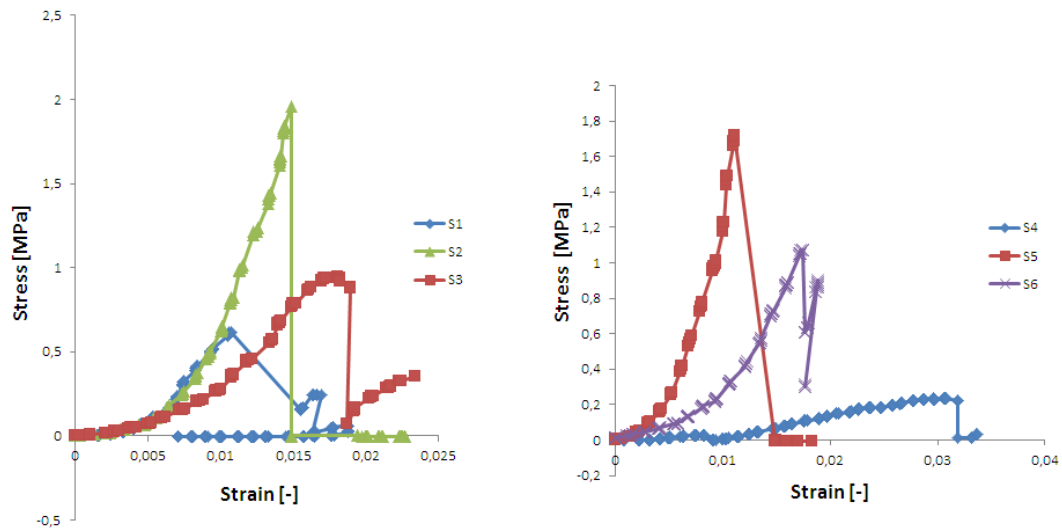
Figure 36: Stress-strain curves for vertical samples (S1-S6), from Svea bay.
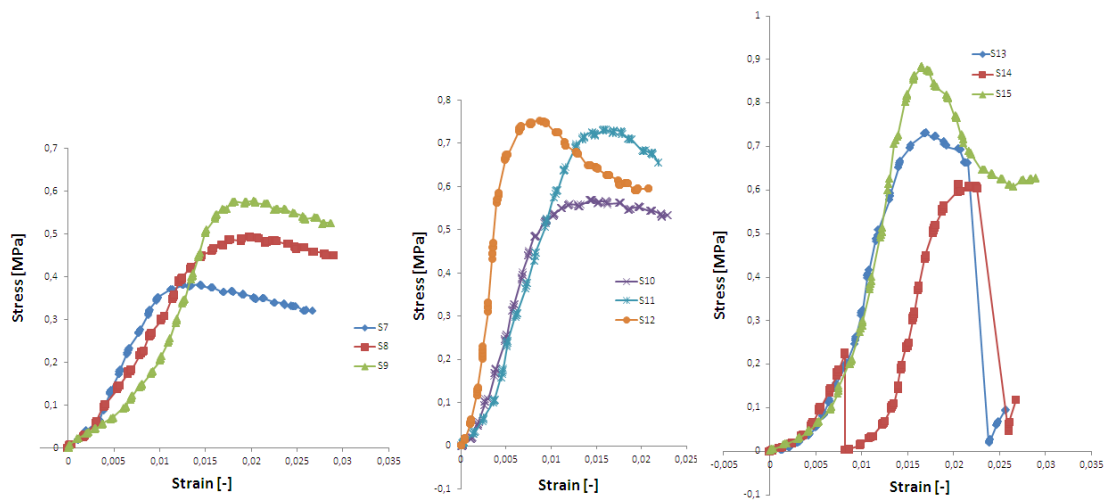
Figure 37: Stress-strain curves for horizontal samples (S7-S15), from Svea bay.

Table 8: Ice properties of compression test samples, Lance

Sample	Time to failure [s]	E [MPa]	σ_C [MPa]
L1	19.1	30.88	0.209
L2	14.9	124.14	0.463
L3	7.3	206.77	0.485
L4	9	149.98	0.439
L5	22	8.86	0.054
L6	12	124.93	0.338
L7	7.9	96.68	0.303
L8	7	50.79	0.243
L9	11.9	55.46	0.289
L10	6.3	64.37	0.175
L11	8.1	47.79	0.183
L12	6	86.98	0.305
L13	21.2	19.71	0.185
L14	*	111.53	0.267
L15	*	58.40	0.336
L16	12.7	24.14	0.129
L17	*	98.39	0.253
L18	*	230.23	0.303
L19	7	73.42	0.235
L20	7	78.94	0.215
L21	*	159.38	0.278
L22	*	43.38	0.205
L23	7	82.37	0.228
L24	10	159.64	0.302
L25	8.2	188.40	0.335
L26	*	71.09	0.196
L27	6	62.34	0.253
L28	7	63.24	0.187
L29	9	97.07	0.337
L30	5	151.46	0.539
L31	11.8	206.52	0.612
L32	11.1	152.20	0.452
L33	7.9	209.70	0.521
L34	14	186.29	0.728
L35	9.3	96.91	0.619
L36	6.9	232.39	0.505
L37	6.1	91.91	0.211
L38	11.8	168.34	0.684
L39	10.2	132.24	0.295
L40	8.4	112.91	0.427
L41	8.1	69.55	0.152
L42	11.9	108.90	0.283

* measurements not avaiable.

Table 9: Mechanical properties for ice core samples used in uniaxial compressive tests, from Svea bay. Dimensions and location is given in table1.

Label	E_T-modul [MPa]	E_S-modul [MPa]	Strength [MPa]	Failure mode	Salinity [‰]
S1	252	259	0.62	ductile	-
S2	775	829	1.96	brittle	-
S3	229	235	0.95	brittle	-
S4	11.2	11.7	0.23	brittle	-
S5	826	911	1.72	brittle	-
S6	137	139	1.07	ductile	-
S7	57.1	57.4	0.38	ductile	5.56
S8	57.8	58.2	0.50	ductile	5.13
S9	73.7	74.3	0.58	ductile	5.28
S10	91.8	92.8	0.56	ductile	5.27
S11	107	108	0.73	ductile	5.14
S12	296	306	0.75	ductile	4.26
S13	154	156	0.73	brittle	5.14
S14	148	150	0.61	brittle	5.30
S15	174	178	0.88	ductile	4.81

4.2   Beam results

The main topic of this thesis is the flexural strength of sea ice covers. The flexural strength may be measured by a cantilever beam test, as discussed previously in section 2.3.2. In order to compare results of elastic modulus measured from compression tests to the beam tests, equation 66 is used.

Figure 47 in appendix A.1 shows a beam element in bending. Elastic modulus in the top fibres at the crack root, for a unit element in bending, can be estimated from the deflection and geometry according to

$$E = \frac{FL^3}{3Iw},\tag{65}$$

here an elastic homogeneous material is assumed($I = bh^3/12$) values for width (b), ice thickness (h) and length to crack root (L) are given in tables 10 and 14, force together with flexural strength is given in tables 11 and 15. By assuming an elastic homogeneous material, bending moment at the crack root is a uni-axial tensile stress in the horizontal direction at the top fibres. Applying Hookes' law, strain can be found according to:

$$\epsilon_b = \frac{\sigma}{E}\tag{66}$$

ϵ_b is given in tables 16 and 12 for the beams in Svea bay and Barents sea.

4.2.1   Beam results Svea bay

In this section results from all beam tests listen in section 3.4 in table 2 are given.

Table 10: Final beam dimensions, Svea bay.

Beam	Length tip-crack root [m]	Length load cell-crack root [m]	Crack length [m]	Ice thickness [m]
C1	3.03	2.97	0.70	0.65
C2	3.40	3.14	0.70	0.76
C3	3.28	3.17	0.70	0.73
Cs1	1.56	1.44	0.68	0.73
Cs2	0.75	0.70	0.70	0.71
Cs3	0.70	0.58	0.72	0.71

Porosity measurements vary with depth and position as well as time. These estimates are based on temperature, density and salinity taken close to the beams at the time the beam tests were performed at depths of half the ice thickness.

Table 11: Beam results, Svea bay

Beam	F_{max} [kN]	$w(F_{max})$ [mm]	σ_F [kPa]	Failure mode
C1	4.151	1.99	250	Quasi-brittle
C2	7.727	2.51	360	Quasi-brittle
C3	4.371	1.80	223	Quasi-brittle
Cs1	12.314	0.60	294	Quasi-brittle
Cs2	24.673	0.07	294	Shear-failure
Cs3	28.442	0.28	273	Quasi-brittle

Table 12: Estimate of elastic modules based on equation 66, Svea bay

Beam	Failure strain [-]	Failure stress [KPa]	E [MPa]	Failure time [s]	Strain rate $[s^{-1}]$
C1	$2.2 \cdot 10^{-4}$	250	1137	0.76	$2.86 \cdot 10^{-4}$
C2	$2.93 \cdot 10^{-4}$	363	1241	1.66	$1.76 \cdot 10^{-4}$
C3	$1.94 \cdot 10^{-4}$	220	1136	1.14	$1.69 \cdot 10^{-4}$
Cs1	$3.16 \cdot 10^{-4}$	293	926.7	1.18	$2.67 \cdot 10^{-4}$
Cs2	$1.27 \cdot 10^{-4}$	294	2297	1.44	$0.89 \cdot 10^{-4}$
Cs3	$4.64 \cdot 10^{-4}$	273	588.5	1.84	$2.52 \cdot 10^{-4}$

Table 13: Porosity of beams, Svea bay

Beam	Brine [‰]	Porosity [‰]	$\sqrt{\nu_b}$
C1	47.7	109.4	0.218
C2	29.1	88.9	0.171
C3	38.7	99.0	0.197
Cs1	44.5	106.1	0.210
Cs2	32.3	106.1	0.180
Cs3	35.8	95.9	0.189
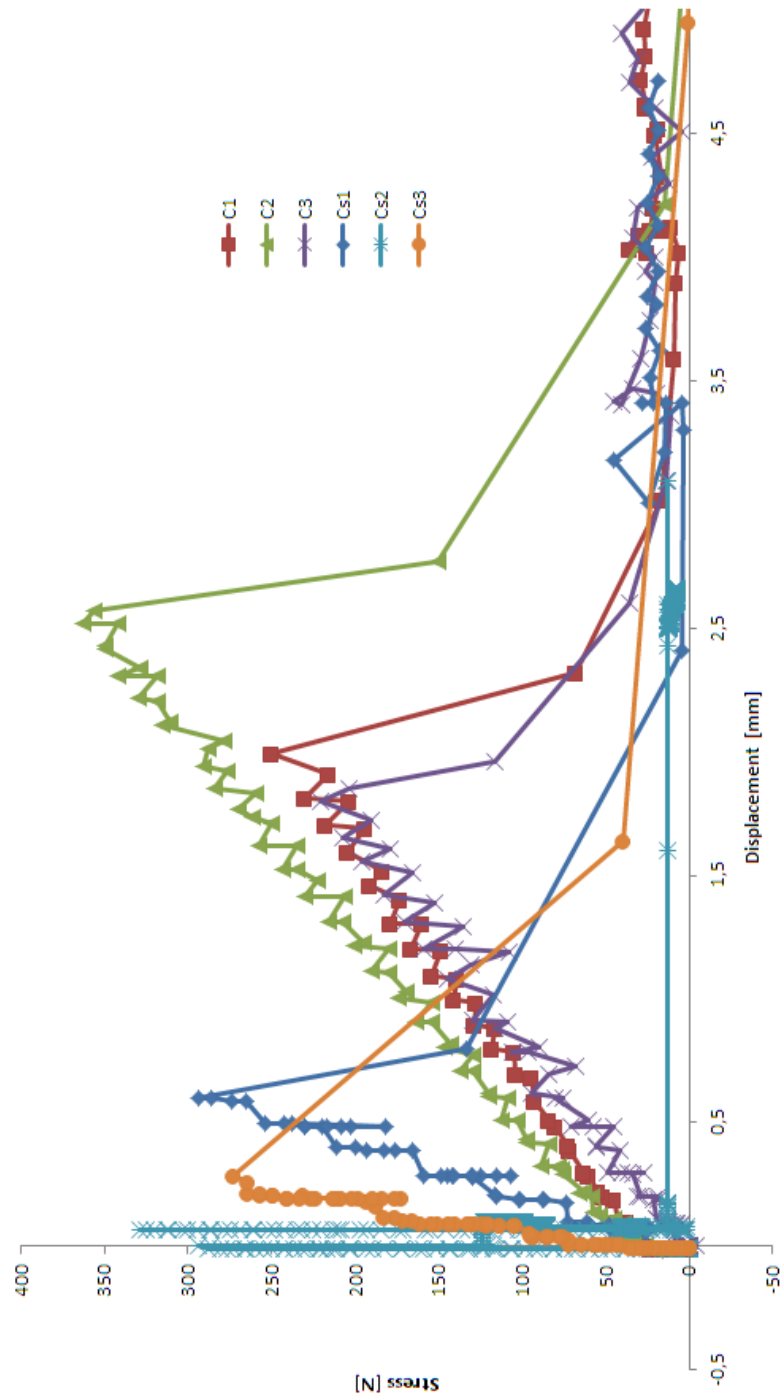
Figure 38: Stress plotted against displacement, Svea bay.

4.2.2 Beam results Lance

Table 14: Final beam dimensions from the Lance-expedition.

Beam	Length tip-crack root [m]	Length load cell-crack root [m]	Crack length [m]	Ice thickness [m]
B1*	2.50	2.30	0.54	0.45
B2**	1.45	1.28	0.53	0.43
B3	2.00	1.80	0.45	0.44
B4	1.90	1.73	0.52	0.45
B5	2.95	2.79	0.53	0.58/0.50***
B6	2.79	2.69	0.60	0.53
B7	3.03	2.87	0.60	0.47

* B1 broke during preperation. ** Load cell was not not centeres. 32cm from left and 18 from right.*** at crack root/load cell

Table 15: Beam results, Lance-expedition

Beam	F_{max} [kN]	$w(F_{max})$ [mm]	σ_F [kPa]	Failure mode
B2	1.663	0.78	130.3	ductile
B3	1.002	1.08	124.3	ductile
B4	1.021	1.78	100.7	ductile
B5	1.425	1.79	154.4	ductile
B6	2.726	1.80	261.2	ductile
B7	1.840	1.92	239.1	ductile

Table 16: Estimate of elastic modules based on equation 66 Lance-expedition

Beam	Failure strain [-]	Failure stress [KPa]	E [MPa]	Failure time [s]	Strain rate [s^{-1}]
B2	$3.07{\cdot}10^{-4}$	130.3	424.4	0.66	$5.12{\cdot}10^{-4}$
B3	$2.20{\cdot}10^{-4}$	124.3	564.6	0.50	$4.40{\cdot}10^{-4}$
B4	$4.02{\cdot}10^{-4}$	100.7	250.7	0.52	$7.72{\cdot}10^{-4}$
B5	$1.47{\cdot}10^{-4}$	154.4	1043	0.70	$2.11{\cdot}10^{-4}$
B6	$1.98{\cdot}10^{-4}$	261.2	1320	1.10	$1.80{\cdot}10^{-4}$
B7	$1.64{\cdot}10^{-4}$	239.1	1455	0.78	$2.11{\cdot}10^{-4}$

Table 17: Porosity of beams, Lance

Beam	Brine [‰]	Porosity [‰]	$\sqrt{\nu_b}$
B2	92.8	92.8	0.305
B3	110.4	110.4	0.332
B4	123.6	123.6	0.352
B5	86.4	86.4	0.294
B6	97.4	97.4	0.312
B7	103.4	103.4	0.322
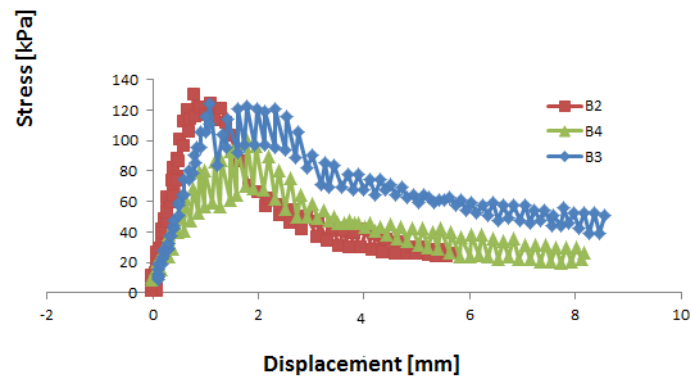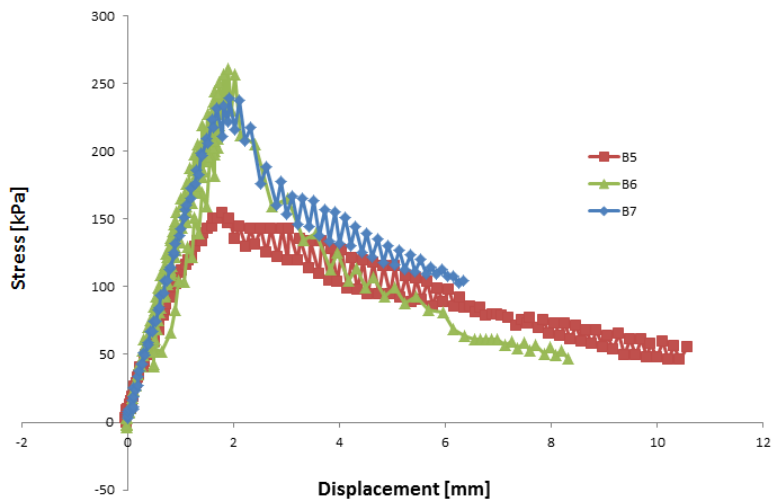
Figure 39: Stress plotted against displacement, Lance expedition.

4.3 Numerical analysis

In this section curve fitting is used to correlate experimentally measured properties. In order to evaluate the quality of fit, goodness of fit it used as a statistical indicator of the quality of the fit. All curve fits are done in Matlab and can be found in the appendix A.2.

Goodness of fit is expressed through r^2, defined as follows for a linear regression model:

$$r^2 = 1 - \frac{SS_{res}}{SS_{tot}}, \tag{67}$$

where $SS_{res} = \sum_i (y_i - f_i)^2$, $SS_{tot} = \sum_i (y_i - \bar{y})^2$, i is the number of samples, y_i denotes sample values, $\bar{y}$ average value and f_i is predicted sample value.

$0 < r^2 < 1$, if $r^2 = 1$ all data points would line on the curve (Walpole, 2007).

4.3.1 Curve fitting compressive strength vs. porosities

We present here compressive data plotted against porosity. Timco and O'Brien (1993) used an exponential function to curve fit flexural strength to root brine fraction. In this chapter the same will be done to the compressive strength data. In theory section 2.2.3 it was shown that strain rate did not show a pronounced effect on tensile and hence flexural strength, thus estimates for flexural strength are not expressed through strain rate. Compressive strength on the contrary is highly dependent of strain rate. Experimental investigations presented in this thesis are although done at the same nominal strain rate of $10^{-3}[s^-1]$ therefore estimates obtained are only a function of brine volume or fraction. Compressive data is curve fitted both to an exponential expression on the form Timco and O'Brien (1993) used, as well as the potential from expressed by Kovacs (1996).

Table 18: Comparison of curve fit parameters

Data	Curve	A	b	r^2
vert.*	$Ae^{\sqrt{\nu_b}}$	6.419 (1.426, 11.41)	-5.549 (-8.849, -2.248)	0.4379
All	$Ae^{\sqrt{\nu_b}}$	9.665 (3.05, 16.28)	-8.475 (-11.38, -5.566)	0.4146
vert.	$A(1 - \sqrt{\frac{v_T}{b}}^{-0.5})^2$	3.636 (-0.7511, 8.023)	745.6 (-674.1, 2165)	0.0799
All	$A(1 - \sqrt{\frac{v_T}{b}}^{-0.5})^2$	2.993 (-0.1969, 6.184)	491.4 (-81.2, 1064)	0.0650

* v= vertical samples from Svea and Lance, All= all samples from Svea and Lance
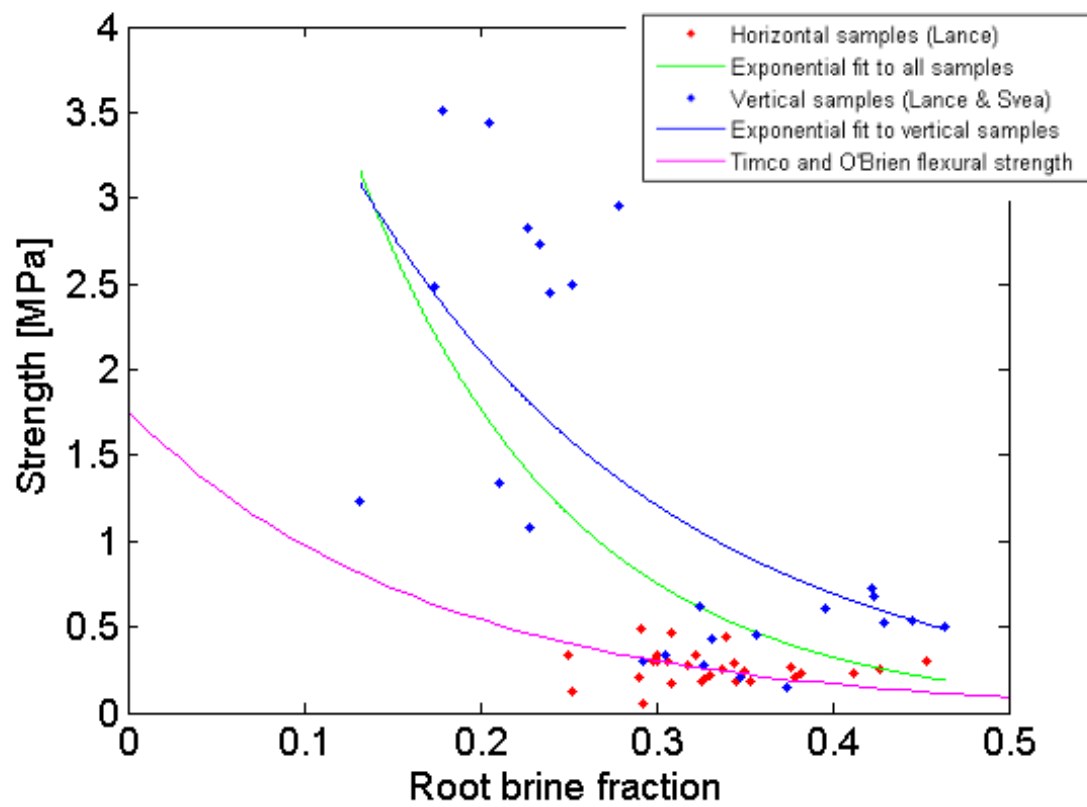
Figure 40: Curve fit of compressive strength vs. root brine fraction according to Timco and O'Brien (1993).
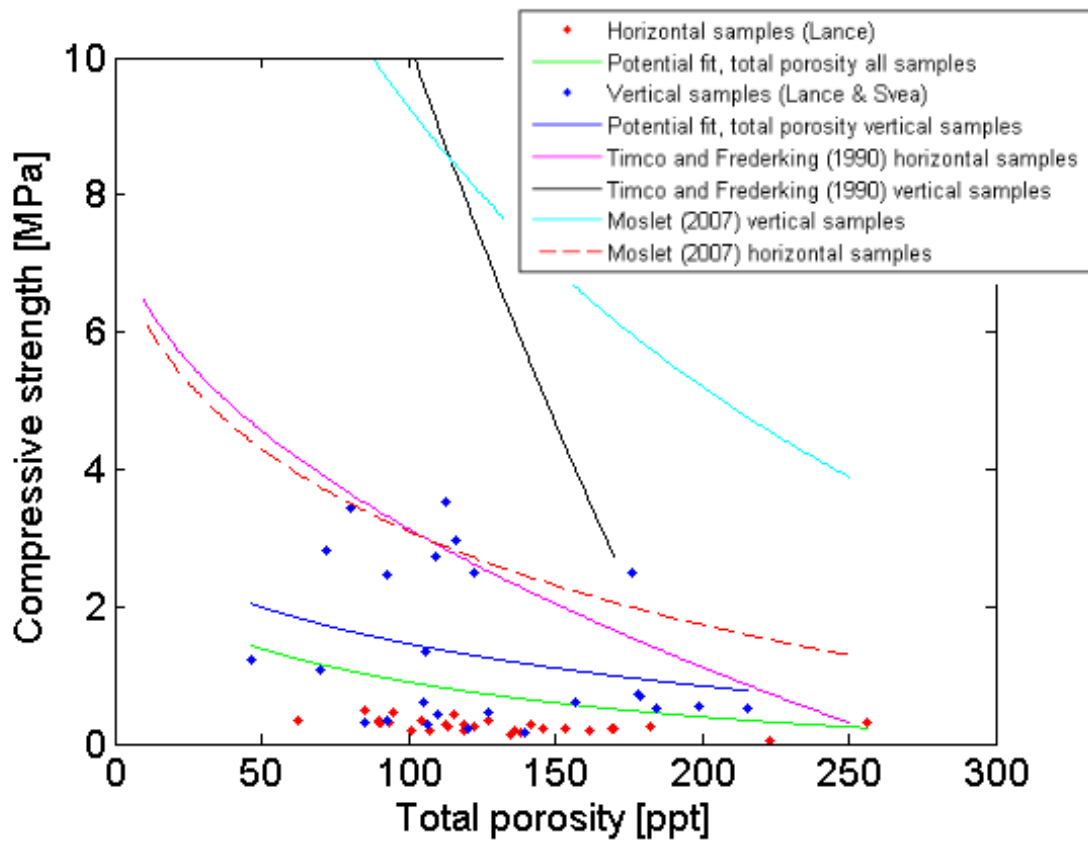
Figure 41: Comparison of curve fits of compressive strength vs. total porosity in ‰, to curve fits done by Moslet (2007) and Timco and Frederking (1990). Fit equation and parameters are given in 18.

4.3.2   Curve fit flexural strength vs. root brine fraction
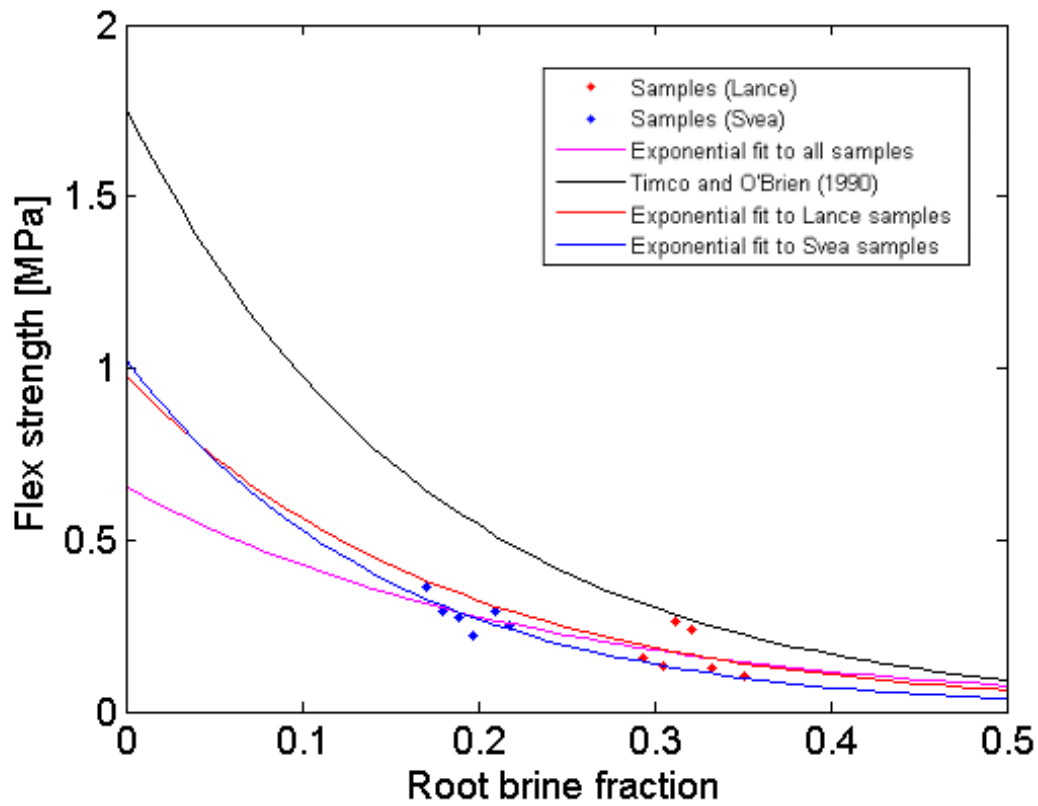
Figure 42: Flexural strength [MPa] vs. root brine fraction.

Table 19: Curve fit of flexural strength vs. root brine fraction

Data	Equation	A	b	r^2
Svea	$Ae^{-b\sqrt{\nu_b}}$	1.028 (-0.9787, 3.034)	-6.689 (-16.89, 3.514)	0.4402
Lance	$Ae^{-b\sqrt{\nu_b}}$	0.9789 (-7.138, 9.096)	-5.526 (-31.76, 20.7)	0.0986
All	$Ae^{-b\sqrt{\nu_b}}$	0.6555 (0.2736, 1.037)	-4.312 (-6.838, -1.785)	0.6267

4.3.3 Curve fitting E(z)

In order to find an estimate for the horizontal elastic modulus E(z), curve fitting using the data from the horizontal compression tests s7-s15 was performed in Matlab. The Matlab code is included in appendix A.2. Equation 63 has five parameters, namely E_0 [MPa], α , the power n, the ice thickness h and distance from the top surface to the neutral axis z_0 (equation 64). E_0 and α are curve fitted with coefficient bounds of 95 %, and n=0.5, n=1 and n=2. Goodness of fit is defined in section 4.3.1, determined by r^2 given in table 20. The fit is based on eight data points (i=8), because sample S12 was neglected to obtain a better fit.

Since equation 63 depends on ice thickness h, and four different ice thickness's were measured in Svea (table 10). E(z) will be calculated for all four thickness's (table 20). Since the shape of all curve fits in table 20 are the same, only one ice thickness figure is shown (figure 43), ice thickness is 0.73 m.
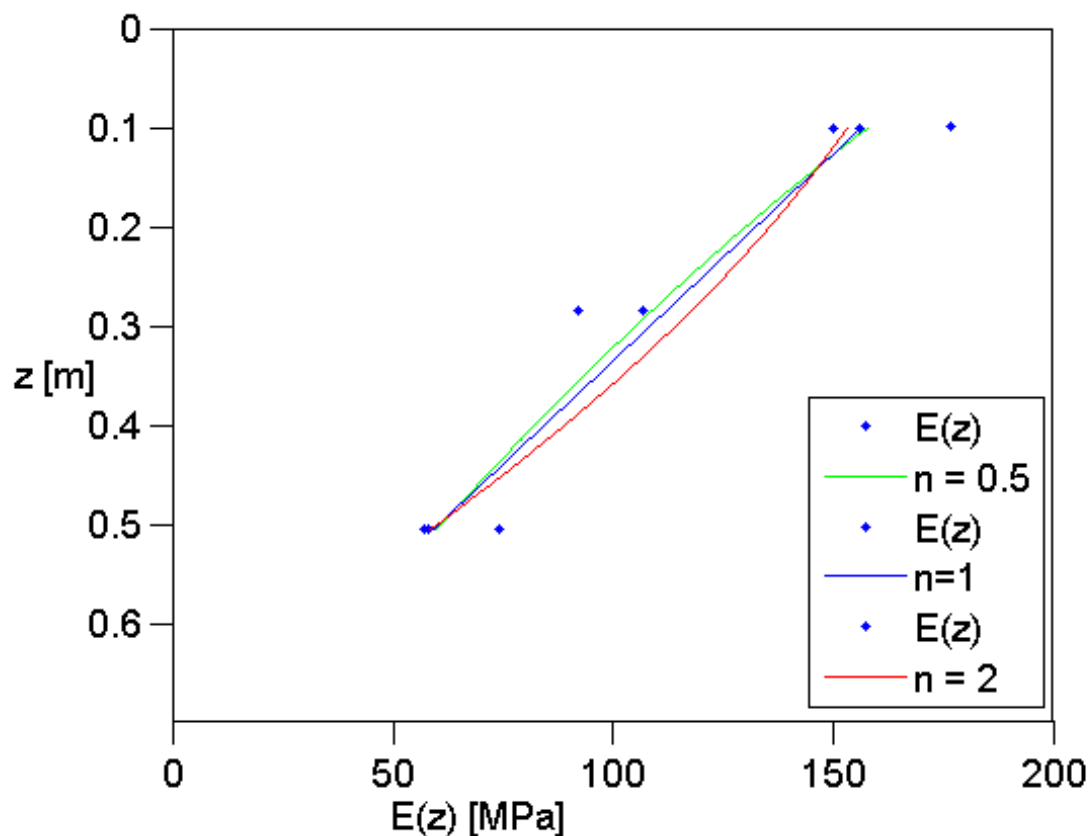
Figure 43: Curve fit of elastic modulus, from Svea bay.Ice thickness 0.73 m.

Experimental values obtained from horizontal uni-axial compression tests of elastic modulus at the two sites on Lance are plotted against depth in figure 44. No curve fit is made for these data, due to the scatter in data points.

Equation 53 is an in-homogeneous equation for flexural strength derived in section 2.3.2, based on an equation for E(z). In table 21, E(z) from equation 63 with

Table 20: Curve fit parameters for elastic modulus, from Svea bay

h [m]	n	α	z_0 [m]	E_0 [MPa]	r^2
	0.5	0.2252	0.2499	370.1	0.9402
0.65	1.0	0.3666	0.2748	246.5	0.9272
	2.0	0.5512	0.2964	184.0	0.8946
	0.5	0.1957	0.2729	378.7	0.9398
0.71	1.0	0.3209	0.2942	251.1	0.9272
	2.0	0.4901	0.3187	186.5	0.8960
	0.5	0.1862	0.2784	381.5	0.9397
0.73	1.0	0.3059	0.3021	252.6	0.9151
	2.0	0.4691	0.3250	187.2	0.8964
	0.5	0.1722	0.2864	388.4	0.9396
0.76	1.0	0.2835	0.3105	254.8	0.9272
	2.0	0.4372	0.3344	188.4	0.8970
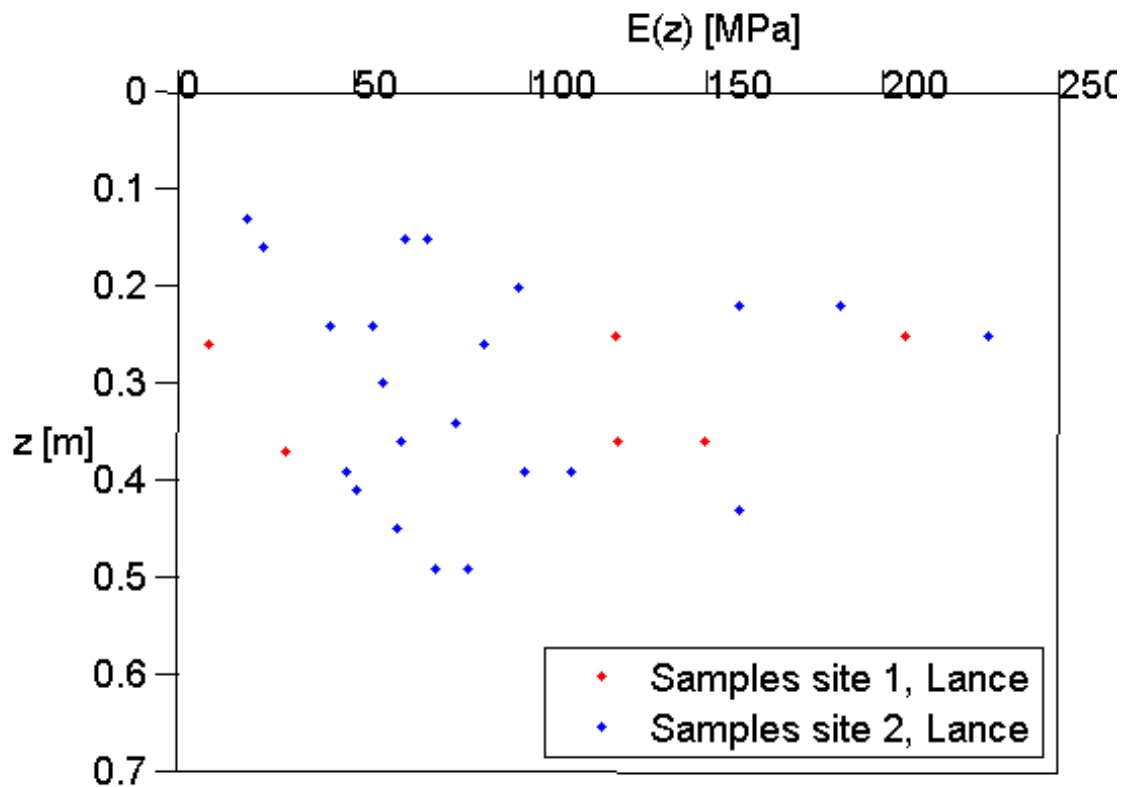
Figure 44: Elastic modulus from compression tests on Lance.

parameters given in table 20 will be used to compare the in-homogeneous equation for flexural strength 53 to the homogeneous equation for flexural strength (equation 51).

Table 21: Comparison of flexural strength calculated with constant E and E(z), for all cantilever beams in Svea.

n		C1	C2	C3	Cs1	Cs2	Cs3
0.5	σ_E [kPa]	250	360	223	293	294	273
0.5	$\sigma_{E(z)}$ [kPa]	440	682	413	545	537	499
0.5	$\frac{\sigma_E}{\sigma_{E(z)}}$	57 %	53 %	54 %	54 %	55 %	55%
1.0	σ_E [kPa]	250	360	223	293	294	273
1.0	$\sigma_{E(z)}$ [kPa]	333	510	310	408	412	383
1.0	$\frac{\sigma_E}{\sigma_{E(z)}}$	75 %	71 %	72 %	72 %	71 %	71%
2.0	σ_E [kPa]	250	360	223	293	294	273
2.0	σ_E [kPa]	285	429	262	345	342	318
2.0	$\frac{\sigma_E}{\sigma_{E(z)}}$	88 %	84 %	85 %	85 %	86 %	86 %

The values for the flexural strength in table 21 is the uni-axial tensile stress in the top ice layer. For the homogeneous ice the stress is linear over the ice thickness, while for the case when the ice is inhomogeneous with E(z) the stress is no longer linearly distributed over the ice thickness. The stress distribution for the three curve fits for cantilever beam C3 is shown in figure 45, curve fit parameters are given in table 20.
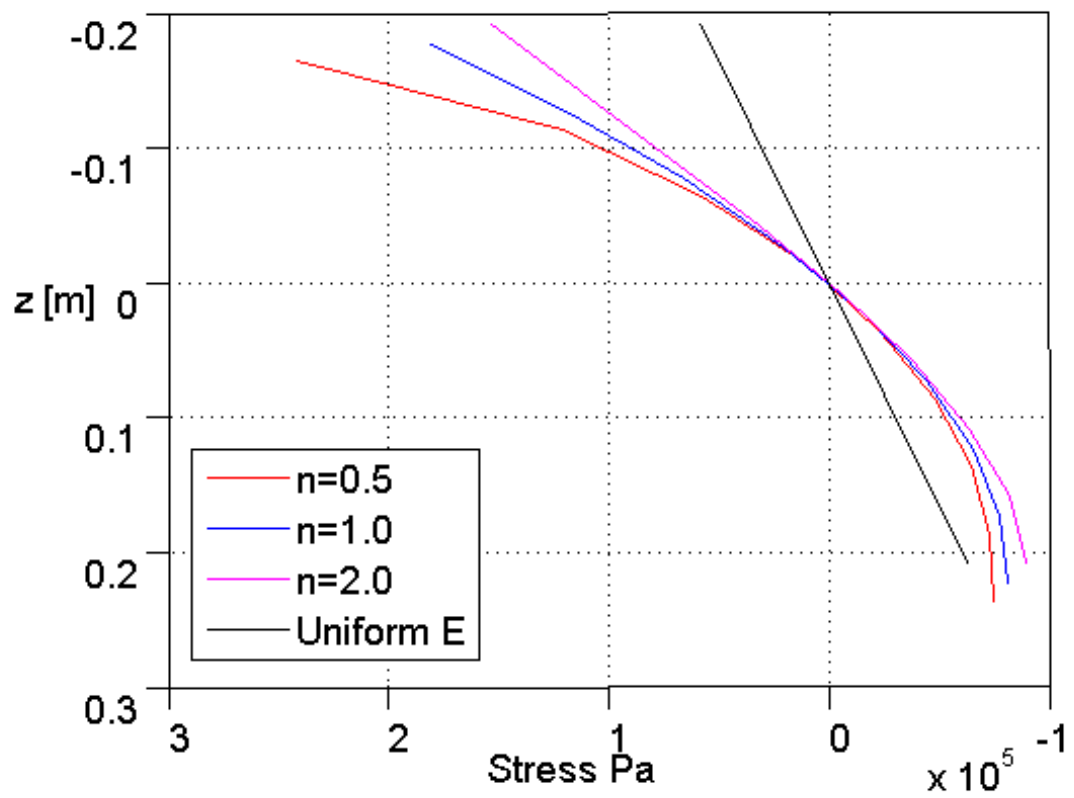
Figure 45: Stress distribution over ice thickness, with E(z) for cantilever beam C3. Curve fit parameters are given in table 20. z=0 is the neutral axis, where the stress is zero.

4.3.4 Beams with Winkler foundation

As stated previously, we wish to study the possible influence of the water support on flexural strength. For this purpose, the Winkler foundation theory is employed. In table 22 stresses for four different cases are shown; the first equation is the standard equation, assuming a uniform elastic modulus E and neglecting the water foundation. In the second equation, the elastic modulus is assumed to vary with depth E(z) according to the equations found by curve fitting in section 4.3.3 (table 20). The third equation assumes a uniform E, but includes the Winkler foundation. At last both the Winkler foundation and a varying E(z) is included. The three latter flexural strength values are compared to the first flexural strength value.

Table 22: Flexural strength derived in four ways. σ (equation 51) with a uniform elastic modulus E. $\sigma_{E(z)}$ (equation 53) with E(z). $\sigma_{winkler}$ (equation 57) with a uniform E and the Winkler foundation. $\sigma_{winklerE(z)}$ (equation 61) with E(z) and the Winkler foundation. The three columns labelled n=0.5,n=1.0 and n=2.0 are for the different E(z) equations (section 4.3.3).

	n=0.5	n=1.0	n=2.0
σ [kPa]	223	223	223
$\sigma_{E(z)}$ [kPa]	413	310	262
$\sigma_{winkler}$ [kPa]	220	220	220
$\sigma_{winklerE(z)}$ [kPa]	406	304	257
$\sigma_{E(z)}/\sigma$	185%	139%	118%
$\sigma_{winkler}/\sigma$	99%	99%	99%
$\sigma_{winklerE(z)}/\sigma$	182%	137%	115%

There are 6 beams with different dimensions and failure loads. In table 22 geometry and failure load from beam test C3 is used (see table 10 and 11).

In table 23 σ and $\sigma_{winkler}$ is calculated for all beams. Elastic modules are taken from the beam test results (table 12 and 16).

Table 23: Comparison of flexural strength calculated with constant E and E(z), for all cantilever beams in Svea.

Beam	C1	C2	C3	Cs1	Cs2	Cs3
σ [kPa]	250.1	360.1	222.8	292.4	293.7	272.7
$\sigma_{winkler}$ [kPa]	249.4	359.4	222.3	292.4	293.7	272.7
E [Mpa]	1137	1241	1136	926.7	2297	588.5
$\sigma_{winkler}/\sigma$	99.8 %	99.8 %	99.8 %	100 %	100 %	100%
Beam	B2	B3	B4	B5	B6	B7
σ [kPa]	130.3	124.3	100.7	154.4	261.2	239.1
$\sigma_{winkler}$ [kPa]	130.2	123.9	100.2	153.7	260.2	237.9
E [Mpa]	424.2	564.6	250.7	1043	1320	1455
$\sigma_{winkler}/\sigma$	99.9 %	99.8 %	99.6 %	99.6 %	99.7 %	99.5%

4.4   Summary

In this section, we have presented the experimental results obtained from two scientific expeditions in Arctic waters, as well as results for curve fitting to these data using expressions from previous authors. The physical properties appears to agree with results Høyland (2009) and flexural strength data points agree with the curve fit Timco and O'Brien (1993). Horizontal uni-axial compression results expands our knowledge of how flexural strength is affected by the distribution of elastic modulus and stresses through the ice thickness. The effect of the water support was also studied.

5 Discussion

Contents

The cantilever beam test, for determining flexural strength, has been thoroughly investigated through the experimental and numerical work presented in the result section (section 4). The main objective of this thesis was to study how spatial variations of elastic modulus and strength, through the ice thickness, affects the flexural strength and how this relates to physical properties. This section will discuss these questions; as is often the case, an answer often prompts new questions.

5.1 Ice properties

5.1.1 Physical ice properties

Temperature measured in Svea bay showed decreasing temperature towards the air surface. Temperature profiles coincides well with what was measured in Van Mijenfjorden by Høyland (2009). Salinity profiles from Svea indicates a c-shape, with higher salinity in the ice boundaries. This suggest brine expulsion towards the top and drainage towards the bottom ice layer.

Temperature profiles taken from ice floes on the expedition to the east coast of Edgeøya in the Barents sea during spring, were more or less uniform at $-2°C$. Although air temperatures barely rose above $0°C$ before mid May (figure 22), solar radiation may have a significant effect on the primary ice layer. Salinity seemed to be lower in the primary ice compared to the secondary ice, indicating desalination and melting.

Gas and brine porosity are physical ice properties calculated from temperature, salinity and density (Cox and Weeks (1983) and Leppäranta and Manninen (1988)). Calculating porosity is important for ice strength. Brine pockets, gas and brine channels are not able to carry shear stresses and cause stress concentrations, reducing the strength in sea ice (Schulson, 1983). Densities measured on the Lance expedition were generally higher compared to Svea (table 5 and 4) a possible explanation is that brine pockets were melting and salt water was kept inside the ice with little drainage. On the Lance-expedition sea water filled all the beam slots before the whole ice thickness was cut, this water could have increased total ice density.

On the other hand, measuring density is generally difficult to perform in field, Timco and Frederking (1995) made a review on density measuring techniques in ice and they found a large scatter in results ranging from 0.72 to 0.94 $[g/cm^3]$. Here a mass/volume technique is used, simply weighting and measuring dimensions of samples. Samples taken out by the Kovacs drill should have a diameter of Ø70mm, however when

weighing and measuring samples in Svea, diameters up to 73 mm were measured. A possible explanation is that brine pockets inside samples froze when exposed to the cold air temperature, increasing the volume and decreasing density. Field hand held spring weights may additionally be temperature dependent and stiffer at low temperatures, decreasing mass and densities measured in Svea compared to Lance. In future works other density measurement techniques should be explored such as the paraffin clod method used for soil density measurements (Howard, 1981).

Grain size measured in the secondary layer of the sea ice on the Lance expedition had a size up to 5 mm with an elongation in the vertical direction, coinciding well with a S2 type sea ice.

5.1.2   Uni-axial compression tests

Uni-axial compression tests have been used to investigate how the elastic modulus and strength varies through the ice thickness. The main points of this part of the discussion are:

1. How elastic properties depends on the test set up, the test machine, and the time to failure.

2. To see how the horizontal elastic modulus varies over the ice thickness, $E(z)$ (equation 63), and how this variation relates to physical properties.

3. Additionally, the importance of the direction of loading will be evaluate by comparing the horizontal and vertical strengths from uni-axial compression tests.

Starting with the first bullet point; Sinha (1983) distinguished time-dependent ice properties from time-independent properties. Because of the time dependence, compressive strength is related to strain-rate. In this thesis a strain rate of $10^{-3}[s^{-1}]$ was used for all tests. Timco and Frederking (1990) point out that high strain rates ($10^{-3}[s^{-1}]$) could lead to premature failure, reducing strength. It is seen from plots in section 4.3.1 (figure 40 and 41) that compressive strength values for low brine contents were well below the predictions made by Moslet (2007) and Timco and Frederking (1990). Indicating that premature failure may have occurred.

Now, by studying the stress-strain curves from the uni-axial compression test results from Svea (in figure 36 and 37) it is clear that the initial slope of the stress-strain curve (the elastic modulus) is almost horizontal. This is the opposite of what would be expected from theory; Sinha (1983) showed that (at time $t = 0s$) the initial slope of the stress-strain curve (the elastic modulus) was the steepest part of the curve. Creep strains would after a short time become significant, decreasing the slope. A possible explanation for the discrepancy, is that initial crushing of sample ends decreases the real initial elastic modulus. From the results it is seen that, after this process is finished, the slope increases up to failure occur. However since there is a time-dependent creep, the elastic modulus would by then have started to decrease. By comparing elastic modulus calculated found from uni-axial compression tests to

those found from beam tests; beam tests show significantly higher values for elastic modulus (table 7, table 8, table 12 and table 16).

Since the discrepancy is seen for all uni-axial compression test results (see figure 36 and 37), the trend for the elastic modulus variation over the ice thickness ($E(z)$) would still be representative, although the absolute values of E may be higher than those found from the uni-axial compression tests.

Moslet (2007) investigated the influence of the test machine stiffness (k_m) on the sample stiffness (k_S). By taking the parallel summation of stiffness's ($1/k_T = 1/k_S + 1/k_m$), a better estimate for the sample elastic modulus can be calculated from $E = k \cdot L/A$ (equation 25). In table 9 the total elastic modulus E_T is compared to the samples elastic modulus E_S. For the horizontal uni-axial compression test results (S7-S15, in table 9) it is however seen that the influence of the test machine stiffness is insignificant. Because of this the total elastic modulus E_T is used as the samples elastic modulus in the rest of the results.

The second bullet point; was to evaluate the effect of physical properties on uni-axial strength and elastic modulus. The effect of temperature variations on both compressive strength and brine is evident; both vertical and horizontal samples taken in the warm ice in spring have higher brine fractions and lower strengths compared to the cold ice samples taken early in March in Svea (summaries in table 4 and 5). For the elastic modulus data found in Svea (figure 43), a pronounced increase in stiffness is seen towards the cold air-surface. The elastic modulus seems to change in the same way as the temperature. This argument is supported by the elastic modules found in the warm ice on Lance; there was a large scatter in data points and no clear variation of $E(z)$ across the ice thickness, this correlates well with the temperature which was uniform over the ice thickness.

The last bullet point; is a statistical evaluation of the difference in compressive and horizontal strength. Since a S2-type sea ice (seen in figure 32) has grains that are elongated in the vertical direction it is suspected that the vertical compressive strength is higher than the horizontal compressive strength. Moslet (2007) did a review where he compared the ratio of σ_v/σ_H, he found a σ_v/σ_h ratio ranging from 1.2 to 4.0. In the following a student-t test, which is a zero hypothesis test, will be used on the compressive strength data (section 4.1.2). The aim is to show that the vertical strength is higher than the horizontal strength with a confidence bound of 95 %.

The zero hypothesis is normally used to determine if two sets of data are significantly different from each other, if the zero hypothesis can be discarded the hypothesis H_1 can be verified by a confidence bound chosen prior to the test. The zero hypothesis (H_0) in this test is that the vertical samples have lower or equal strengths compared to horizontal samples. The confidence interval is set to $\alpha = 95\%$ coinciding with a t-critical value t_{cr} depending on the degree of freedom, if $t > t_{cr}$ the H_0 hypothesis can be discarded. For details of the test a review in Walpole (2007) is recommended.

$$H_0 : \mu_h \leq \mu_v$$
$$H_1 : \mu_v > \mu_h,$$

(68)

where μ_h is the real average compressive strength of a horizontal ice sample and μ_v the real vertical strength.

$$t = \frac{X_v - X_h}{\sqrt{\frac{s_h^2}{n_h} + \frac{s_v^2}{n_v}}}, \tag{69}$$

where X_v is the average vertical strength, X_h is the average horizontal strength, s_h is the standard deviation of the horizontal strengths, s_v is the standard deviation of the vertical strength, n_v and n_h is the number of samples in the vertical and horizontal direction respectively.

Based on the compressive strength results from the Lance expedition the data in table 24 is obtained:

Table 24: Comparing vertical and horizontal strength, Lance

Orientation	X [MPa]	s[MPa]	n number of samples
Horizontal	0.264	0.093942	29
Vertical	0.455	0.178384	14

With the smallest number of samples equal 14, the degree of freedom is $d = n - 1 = 13$ corresponding to $t_{cr} = 2.160$. Based on table 24 the t-value is 3.76 which is larger than the critical value and hence; the zero hypothesis can be discarded. Meaning that with a 95 % certainty average vertical strength is higher than average horizontal strength.

Based in the compressive strength results found in the Svea bay the data in table 25 is calculated:

Table 25: Comparing vertical and horizontal strength, Svea

Orientation i	X [MPa]	s[MPa]	n number of samples
Horizontal	0.637	0.151972	9
Vertical	1.866	1.030893	18

With the smallest number of tests equal 9, the degree of freedom is $d = n - 1 = 8$, this corresponds to $t_{cr} = 2.306$. The t-value was calculated to 2.78 which is larger than the critical value, hence the zero hypothesis can be discarded. With a 95 % certainty average vertical strength is higher than average horizontal strength.

5.2 Beam tests

The main scope of this thesis is the cantilever beam test, used to determine flexural strength. The study of how spatial variations of elastic modulus and strength throughout the ice thickness affects the average flexural strength of a sea ice cover, and how this relates to physical ice properties will be discussed in this section. The significance of the water foundation will also be deliberated.

5.2.1 Elastic modulus and flexural strength

Uni-axial compression tests were used to determine how the elastic modulus varied over the ice thickness. In the cold ice in Svea, there was an evident correlation between ice depth and elastic modulus (figure 43). For the warm ice on Lance no such effect was seen (figure 44). This indicated a coherence between the elastic modulus and the temperature profile. In this part of the discussion, the following bullet points will be deliberated:

1. How a varying $E(z)$ effects the stress distribution $\sigma(z)$ and the flexural strength $\sigma(z = 0)$, as well as the failure mode.

2. The importance of the shape of E(z) will be evaluated.

3. The influence of the brine volume and beam size on the flexural strength.

4. Finally, some remarks on possible consequences $E(z)$ and $\sigma(z)$ may have for structural design.

For the cold ice in Svea curve fits were made based on the presumed equations (equations 63) in Kerr and Palmer (1972). The authors declare little of what they based their equations on, expect one sentence stating that "*An early attempt to take into consideration the effect of varying temperature across the plate thickness was presented in 1943.*" They probably based the shape of E(z) on a fictitious temperature profile. They further argued that if E(z) varied across the ice thickness, and that the stress distribution was not linear. This is clearly seen from the stress distribution in figure 45. If the ice is stiffer in the top layer than the bottom layer, the maximum tensile stress e.g. the flexural strength becomes significantly larger than the average flexural strength calculated from a linear stress distribution. Also it is seen that the neutral axis is moved upwards e.g. the tensile stress is distributed over a smaller portion of the cross section area than the compressive stress. This might indicate that the failure zone in cold ice is smaller than for the failure zone in warm ice, supporting the presumption of brittle failure in cold ice and quasi-brittle failure with softening in warm ice. This means that the decrease in the stress-strain

curve upon failure seen for warm ice is probably the material behaviour, and not boundary effects from the surrounding ice sheet (given from the stress-displacement plots in figures 39).

Now regarding the shape E(z). Three different curve fits for E(z) were compared in the result section. The largest deviation between the average flexural strength found from the linear stress distribution and the flexural strength found from a non-linear stress distribution, was for $n = 0.5$. Using E(z) with $n = 0.5$ gave nearly twice the flexural strength compared to the flexural strength obtained with a uniform E (see table 21).

Goodness of fit evaluations seemed to suggest that the power $n = 0.5$ gave the best fits to the data, with $r^2 = 0.94$. Curves for E(z) when $n = 0.5$ also seemed to coincide best with the temperature profiles T(z) found in Svea, compared to $n = 2.0$ and $n = 1.0$ (figure 27).

The influence of brine fraction on strength was also studied. Timco and O'Brien (1993) expressed the correlation between flexural strength and brine with the equation $\sigma_f = 1.76e^{-5.88\sqrt{\nu_b}}$. Curve fitting of the results of flexural strength expressed by the root brine fraction was shown in section 4.3.2. The data from Lance were more or less on the line found by Timco and O'Brien (1993), results from Svea on the other hand were a bit below what would be expected. If the flexural strength results with a varying elastic modulus (and $n = 0.5$) is plotted, it seems to be a better correlation with the equation used by Timco and O'Brien (1993) (figure 46). However the black data points in figure 46 are based on average values for flexural strength, for comparison the average flexural strength from Svea should also be used, because of the limited amount of data also these points seem to be within what Timco and O'Brien (1993) found.

The size difference of flexural strength was studied in Svea. Beams of dimensions much shorter than what was recommended by Kämäräinen (1993) were tested. However no apparent size effect was found. Shear failure and size effects should be further investigated in future works.

As a final remark, the importance of these results on structural design will briefly be discussed. The average flexural strength of ice sheets seems to be similar for warm and cold ice. The bending moment at failure, does not show any significant difference from either the size of the beam nor the temperature. However the failure mode for cold ice seems to be brittle and for warm ice ductile. A brittle failure takes less time than a ductile failure as the stress drops instantly. This means that the energy stored in the material is released faster than for a ductile failure. As a result an impact form a cold ice sheet may cause more damage on a structure than an impact from a warm ice sheet. The effect of a varying $E(z)$ for structural design should be studied more apprehensively. Additionally; since cold ice seems to be softer and weaker in the bottom than the top layer (see figure 37), the effect of applying the load from underneath the beam should be studied. For this analysis another yield surface than Von Mises (Drucker-Prager of Mohr-Coulumb) shown be employed in order to describe the different behaviour of ice in compression an tension.
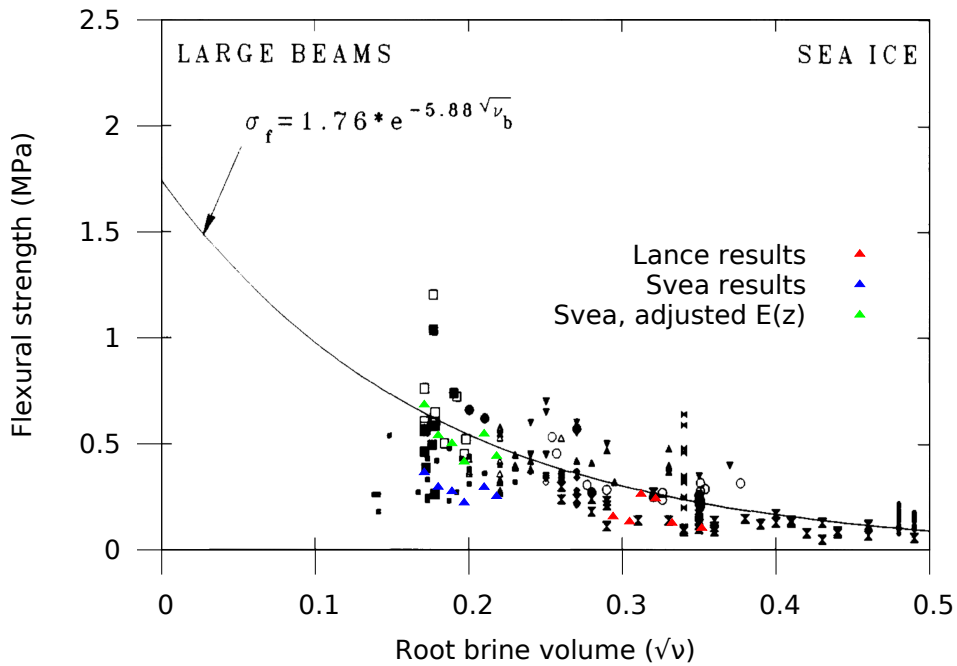
Figure 46: Flexural strength data plotted on top of flexural strength formula and data found by Timco and O'Brien (1993). About the plot; when looking at the marks on the axes the marks inside of the figure frame are from figure 11 and those outside the figure frame are from the data found from this work e.g. the points are correctly placed.

5.2.2 The Winkler foundation

In this thesis the Winkler foundation has been used, to investigate the importance of the distributed force from the water on the cantilever ice beam. The elastic Winkler foundation was first introduced by Winkler in 1867 (Hetenyi, 1946). Originally it was used to study how railway tracks, supported by soils, deflect by passing trains. If the soil stiffness (k) was low, large deflections were found in the rails. However soil stiffness is, in most cases, significantly higher than the stiffness of water (the buoyancy). The force distribution from the Winkler foundation is; $F(x) = kw(x)$. Free end deflections found from the experimental beam tests were all less than $2mm$ (table 11 and table 15), indicating that the contribution from the water force is low.

From equation 57, it can be seen that the bending moment and hence the flexural strength is dependent on β. β is the relation between the moment of inertia (I), the elastic modulus (E)and the stiffness of the water (k the buoyancy); $\beta = \sqrt[4]{k/4EI}$.

An increase in β corresponds to a reduction in strength. Since β is a fourth order root, a reduction in flexural strength would in practice mean a significant decreasing in ice thickness or ice stiffness.

From experimental results of beam tests in both Svea and on Lance flexural strength including the Winkler foundation was calculated (in section 4.3.4). The analytical

investigation showed that flexural strength calculations, including the Winkler foundation, were all 99% of the flexural strength obtained when the Winkler foundation was neglected. Additionally the contribution from the water foundation on flexural strength, was compared to the contribution of a varying elastic modulus through the ice thickness ($E(z)$) seen in table 22. This showed that the decrease in flexural strength caused by the water foundation, was much lower than the increase in flexural strength from a varying elastic modulus. As a result the water foundation can be neglected from calculations of the flexural strength in floating ice beams.

6   Conclusion

Experimental and numerical investigations of beam tests in floating sea ice covers has been performed to study how spatial variations of ice properties affects the average flexural strength of ice sheets. Two scientific expeditions were designed and executed in cooperation with the SMIDA-group and UNIS students (course AT-211). The first expedition took place from the 05th to the 16th of March 2013 in Svea bay in Van Mijenfjorden on Spitsbergen. The second expedition took place on the research vessel Lance, travelling to the sea ice east of Edgeøya in the Barents sea, from the 25th of April to the 04th of May 2013. Sixs cantilever beam tests, temperature, salinity, porosity and uni-axial compression tests were conducted on both expeditions.

Experimental results from the sea ice found in Svea showed a pronounced decrease in temperature towards the cold air surface, while the horizontal elastic modulus showed a significant increased towards the air surface; e.g. the upper ice layer was stiffer than the lower ice layer. From numerical analysis elastic modulus, expressed by equation $E(z) = E_0[1 - (1-\alpha)(\frac{z}{h} + \frac{z_0}{h})^n]$, was fitted to the experimental data. The data was compared to three different n-values; $n = 2.0$, $n = 1.0$ and $n = 0.5$. Goodness of fit calculations showed that the power $n = 0.5$ gave the best prediction of $E(z)$, additionally for $n = 0.5$ temperature profiles and $E(z)$ were similar. The impact of a varying $E(z)$ was a non-linear stress distribution where the maximum tensile stress e.g. the flexural strength became significantly higher than the average flexural strength calculated from a linear stress distribution. Additionally the tensile stress was distributed over a smaller portion of the ice thickness than the compressive stress.

Experimental results from the sea ice on Lance showed a uniform temperature distribution across the ice thickness at a temperature of approximately -2 $^\circ C$. No apparent relation for elastic modulus variation through the ice thickness was found, supporting that elastic modulus is mainly dependent on temperature.

Numerical calculations of the impact of the water foundation on the flexural strength showed that; the flexural strength including the Winkler foundation was 99 % of the flexural strength calculated when the Winkler foundation was excluded. It was therefore concluded that the water foundation could be excluded from flexural strength calculations.

References

Assur (1958). Composition of sea ice and it's tensile strength. *Technical Report U.S. National Academy of Science.* 106p-138p. (-> page 10).

Bazant and Planes (1998). *Fracture and size effect in concrete and other quasibrittle materials.* CRC press. ISBN 0-8493-8284-X,616p. (-> page 21).

Bernal and Fowler (1933). A theory of water and ionic solution, with particular reference to hydrogen and hydroxyl ions. *THe journal of chemical physics*, (8). 515p-549p. (-> page 6).

Cook and Young (1999). *Advanced mechanics of materials.* Prentice Hall. ISBN 0-13-396961-4,715p. (-> pages vi, vii, 27, 28, 28, 79, and 82).

Cox and Weeks (1983). Equations for determining the gas and brine volumes in sea ice samples. *journal og Glaciology*, (Vol. 29,No.102). 306p-316p. (-> pages 8, 9, 9, 10, and 65).

Ervik Åse, Pedersen Cathrine Yvonne, G. N. S. D. A. S. E. (2012). Cold lab week 44 report. Technical report, UNIS. (-> pages vi, vi, vi, vi, 8, 8, 9, and 34).

Gabrielsen, Barrault, Caline, and Høyland (2008). Comparison of physical and mechanical properties of coastal ice and level ice. *19th IAHR International Symposium on Ice*, (-). -. (-> page 12 and 12).

Hetenyi (1946). *Beams on elastic foundation.* University of michigan studies. 624.072.233.5H47b, 255p. (-> pages 71 and 82).

Hirayama, e. a. (1990). Parametric expressions for ice compressive and flexural strength. *Helsinki University of Technology, Espoo, Finland, FI, Finland.* (-> page 26).

Hobbs (1974). *Ice Physics.* ISBN 0198519362. (-> pages vi, 7, and 7).

Holm, C. A. (2010). Lecture notes tkt4124. Technical report, NTNU. (-> pages vi and 22).

Howard, Richard F.; Singer, M. J. (1981). Measuring forest soil bulk density using irregular hole, paraffin clod, and air permeability. *Society of American Foresters*, (2). 316p-322p. (-> page 66).

Høyland (2009). Ice thickness, growth and salinity in van mijenfjoden, svalbard, norway. *Polar research*, (No 28). 339p-352p. (-> pages vi, 3, 10, 10, 10, 11, 11, 11, 12, 31, 64, and 65).

Kerr and Palmer (1972). The deformation and stresses in floating ice plates. *Acta Mechanica 15.* 57p-72p. (-> pages vi, 3, 25, 29, 29, 30, and 70).

Kämäräinen, J. (1993). *Studies on ice mechanics.* ISBN 951-22-1550. (-> pages vi, 5, 5, 7, 8, 8, 11, 11, 12, 25, and 71).

Kovacs (1996). Estimating the full-scale tensile, flexural, and compressive strength of first-year ice. *CRREL*, (11). part 2. (-> page 55).

Lemaitre and Chaboche (1990). *Mechanics of soild materials*. ISBN 0-521-47758-1. (-> pages 12 and 14).

Leppäranta and Manninen (1988). The brine and gas content of sea ice with attention to low salinities and high tempeatures. *Technical report*, (Finnish Inistitute of marine research). 14p. (-> pages 8, 9, and 65).

Marchenko (2012). Lecture notes at-332, at-332. Technical report. 14 parts. (-> pages vi and 6).

Marchenko, e. a. (2011). Field studies of sea water and ice properties in svalbard fjords. *POAC11-148*. (-> pages 5 and 25).

Moslet (2007). *In-situ measurments of sea-ice parameters that affect the loads on coastal and offshore structures*. PhD thesis, Norwegian University of Science and Technology, The University Centre in Svalbard. 144p. (-> pages vii, 16, 17, 34, 34, 46, 57, 66, 67, 67, and 84).

Petremko and Whitworth (1993). *Physics of ice*. ISBN 0-19-8518951. (-> page 6).

Pounder (1965). The physics of ice. *Oxford Pergamon press Library of Congress Catalog*, (No. 65-21141). 151p. (-> page 9).

Sanderson (1988). *Ice Mechanics and Risks to Offshore Structures*. (-> pages vi, 14, 14, 15, 16, 17, 20, and 21).

Schulson (1983). The structure and mechanical behavior of ice. *JOM*, (51(2)). 21p-27p. (-> pages vi, 17, 17, 18, and 65).

Schwarz, e. a. (1981). Standardized testing methods for measuring mechanical properties of ice. *Cold Regions Science and Technology*. 245p-253p. (-> pages vi, 25, 26, 26, 26, and 26).

Sinha (1981). Constant stress rate deformation modulus of ice. *POAC 81*, (Vol 1). 216p-224p. (-> page 14, 14, 14, and 14).

Sinha (1983). Creep model of ice for monotonically increasing stress. *Colad region science and techonlogy*, (8). 25p-33p. (-> pages 14, 66, and 66).

Sinha and Frederking (1979). Effect of test system stiffness on strength of ice. *POAC79*, (873). 708p-717p. (-> pages 18, 19, and 20).

Sinha and Nakawo (1981). Growth of first year sea ice, eclipse sound, baffin island, canada. *National Reseach Council of Canada*, (No 28). 339p-352p. (-> pages vi, 10, 12, and 13).

Sodhi (1995). Wedging action during vertical penetration of floating ice sheets. *AMD-vol. 207, Ice Mechanics ASME 1995*. 65p-80p.

Timco and Frederking (1990). Compressive strength of sea ice sheets. *Cold Regions Science and Technology*, (17). 227p-240p. (-> pages vii, 16, 17, 17, 57, 66, 66, and 84).

Timco and Frederking (1995). A review of sea ice density. *Cold regions science and technology.* 1p-6p. (-> page 65).

Timco and O'Brien (1993). Flexural strength equation for sea ice. *Cold Regions Science and Technology*, (22). 286p-298p. (-> pages vi, vi, vi, vii, vii, 3, 18, 18, 19, 19, 21, 25, 55, 55, 56, 64, 71, 71, 71, 71, 72, and 83).

Timco and Weeks (2009). A review of the engineering properties of sea ice. *Cold Regions Science and Technology.* 108p-118p. (-> page 5).

Walpole, e. a. (2007). *Probability and Statistics for Engineers and Scientists.* ISBN-10: 0131877119. (-> pages 55 and 67).

Zumdahl (2009). *Chemical principles.* ISBN 0538734566. (-> page 6 and 6).

A Appendix

A.1 Winkler foundation derivation

For the derivation on the Winkler foundation a classical beam theory is used, the following assumptions are made:

- A linear elastic material which follows Hooke's law (equation 70)

- Small deflections

- According to section 2.2.4 the elastic modulus is assumed vary in the z-direction $E(z)$

$$\sigma_{xx} = \epsilon_{xx} E(z) \tag{70}$$
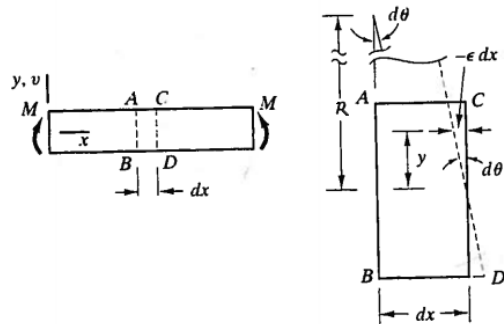
Figure 47: Beam element, curved due to bending, on page 13 Cook and Young (1999)

Deflections are assumed to be small corresponding to a small curvature and a small angle θ seen in figure 47. It can be shown by taking the limit of the Taylor series of sine and cosine that $\sin(\theta) \approx \theta$ and that $\cos(\theta) \approx 1$ giving the following expression for tangent of the angle θ : $\tan(\theta) = \frac{sin(\theta)}{cos(\theta)} \approx \frac{\theta}{1}$ this leads to the following expression for the angle of the element in figure 47:

$$d\theta = \frac{-\epsilon_{xx} dx}{z} \tag{71}$$

$$d\theta = \frac{dx}{R} \tag{72}$$

combining the two equations give the following

$$\frac{d}{dx}\theta = \frac{-\epsilon_{xx}}{z} \tag{73}$$

From figure 47 the angle of rotation $\theta = \frac{d}{dx}w(x)$ where $w(x)$ is the deflection as a function of the x-position on the beam. This gives the following:

$$\frac{d}{dx}\theta = \frac{-\epsilon_{xx}}{z} = \frac{d^2}{dx^2}w(x) \tag{74}$$

Now by using Hookes law (equation 70) on the from $\epsilon_{xx} = \frac{\sigma}{E(z)}$ and the formula for the bending moment $\sigma = \frac{M_x}{I_1}zE(z)$ according to equation 49. Where the modified moment of inertia is given as:

$$I_1 = \int\limits_{-b/2}^{b/2} \int\limits_{-z_0}^{h-z_0} z^2 E(z)dydz = b\int\limits_{-z_0}^{h-z_0} z^2 E(z)dz \tag{75}$$

$$\frac{-\epsilon_{xx}}{z} = \frac{d^2}{dx^2}w(x) = \frac{-\frac{M_x}{I_1}zE(z)}{E(z)z} \tag{76}$$

gives the following

$$-M_x = I_1\frac{d^2}{dx^2}w(x) \tag{77}$$

The derivatives on the moment and shear force is used in the final steps of the derivation of the beam equation 80 $\frac{d}{dx}M_x = V$ and $\frac{d}{dx}V = kw(x) - q(x)$

$$-\frac{d}{dx}M_x = I_1\frac{d^3}{dx^3}w(x) \tag{78}$$

$$-\frac{d}{dx}V = I_1\frac{d^4}{dx^4}w(x) = kw(x) - q(x) \tag{79}$$

$$I_1\frac{d^4}{dx^4}w(x) + kw(x) = q(x) \tag{80}$$

There is no distributed force $q(x)$ in the ice cantilever beam problem

$$I_1\frac{d^4}{dx^4}w(x) + kw(x) = 0 \tag{81}$$

An analytic solution of equation 81 emerges from the boundary conditions for the given problem.

The problem solved is a cantilever beam with an end point load, which give the following boundary conditions:

- $w(0) = 0$

- $\theta(0) = 0 = \frac{\mathrm{d}}{\mathrm{dx}}w(0)$

- $M(L) = 0 = I_1\frac{\mathrm{d}^2}{\mathrm{dx}^2}w(L)$

- $V(L) = -F = -I_1\frac{\mathrm{d}^3}{\mathrm{dx}^3}w(L)$

Equation 81 is a homogeneous ordinary differential equation of fourth order, it can be solved when boundary conditions are known. By assuming a solution on the form $w = e^{rx}$ and writing equation 81 on the form

$$\frac{\mathrm{d}^4}{\mathrm{dx}^4}w(x) + \frac{k}{I_1}w(x) = 0 \tag{82}$$

By substituting $w = e^{rx}$ into equation 82 and by solving the characteristic forth order differential equation:

$$m^4 = \frac{-k}{I_1} \tag{83}$$

With the complex roots:

$$m_1 = -m_3 = \sqrt[4]{\frac{k}{4I_1}}(1 + i) = \beta(1 + i) \tag{84}$$

$$m_2 = -m_4 = \sqrt[4]{\frac{k}{4I_1}}(-1 + i) = \beta(-1 + i) \tag{85}$$

where

$$\beta = \sqrt[4]{\frac{k}{4I_1}} \tag{86}$$

This gives the general solution:

$$w(x) = A_1e^{m_1 x} + A_2e^{m_2 x} + A_3e^{m_3 x} + A_4e^{m_4 x} \tag{87}$$

Using the correlations between the harmonic and the exponential function:

$$e^{i\beta x} = \cos \beta x + i \sin \beta x \tag{88}$$

$$e^{-i\beta x} = \cos \beta x - i \sin \beta x \tag{89}$$

Now also by introducing the following new constants:

$C_1 = (A_1 + A_4)$, $C_2 = (A_1 - A_4)$, $C_3 = (A_2 + A_3)$ and $C_2 = (A_2 - A_3)$ we get the following final expression for the displacement as a function of the position x:

$$w(x) = e^{\beta x}(C_1 \cos \beta x + C_2 \sin \beta x) + e^{-\beta x}(C_3 \cos \beta x + C_4 \sin \beta x) \tag{90}$$

With the boundary conditions above the system can be solved to find the particular case for a cantilever beam loaded with a point load in the free end.

Using the correlations for the hyperbolic functions and the exponential:

$$\sinh \beta = \frac{e^{\beta x} - e^{-\beta x}}{2} \tag{91}$$

$$\cosh \beta x = \frac{e^{\beta x} + e^{-\beta x}}{2} \tag{92}$$

From these relations and the boundary conditions given in A.1 the final formula for the deflection is:

$$w(x) = \frac{2F\beta}{k} \frac{\sinh \beta x \cos \beta (L-x) \cosh \beta L - \sin \beta x \cosh \beta (L-x) \cos \beta L}{\cosh^2 \beta L + \cos^2 \beta L} \tag{93}$$

At the free end where $x = L$ and applying that $\sin(\beta x)\cos(\beta x) = \sin(2\beta x)$ and $\sinh \beta x \cosh \beta x = \sinh 2\beta x$ the following expression for the end deflection emerges:

$$w(L) = \frac{F\beta}{k} \frac{\sinh 2\beta L - \sin 2\beta L}{\cosh^2 \beta L + \cos^2 \beta L} \tag{94}$$

The momentum at the fixed end is found from setting $x = 0$ in equation 77 and from differentiating equation 94 twice, the momentum becomes:

$$M(0) = \frac{-F}{\beta} \frac{\sinh \beta L \cos \beta L + \cosh \beta L \sin \beta L}{\cosh^2 \beta L + \cos^2 \beta L} \tag{95}$$

Formulas were found and checked against Cook and Young (1999) and Hetenyi (1946).

A.2 Matlab code

A.2.1 Curve fits of compression strength vs. porosity

With this curve fit the data from the compressive strength tests were compared to an exponential expression on the form Timco and O'Brien (1993) shown in figure 40.

```matlab
1  clc
2  clear all
3  close all
4
5  %data of comp. strength of all samples
6
7  load strporo1.dat
8  z1 = strporo1(:,1);
9  y1 = strporo1(:,2);
10
11 [sig2, gof2]=fit(y1,z1,'exp1')
12
13
14 opts = fitoptions( sig2 );
15 opts.Display = 'Off';
16 opts.Lower = [0 0.05 ];
17 opts.StartPoint = [0.9706 0.957166948242946];
18 opts.Upper = [Inf Inf];
19
20
21 f=plot(sig2,'g',y1,z1,'r.');
22 hold on
23
24 %data of comp. strength of vertical samples,
25   Svea and Lance
26 load strporo.dat
27 z = strporo(:,1);
28 y = strporo(:,2);
29
30 [sig,gof]=fit(y,z,'exp1')
31
32 opts = fitoptions( sig );
33 opts.Display = 'Off';
34 opts.Lower = [0 0.05 ];
35 opts.StartPoint = [0.9706 0.957166948242946];
36 opts.Upper = [Inf Inf];
37
38 h=plot(sig,'b',y,z,'b.');
39 hold on;
40
41 %legend([h,f],'Vertical samples: Lance and Svea',
42   'Exponential fit', 'All samples: Lance and Svea',
43    'Exponential fit')
44
45 t=0:0.01:0.5;
46
47 i=1.76*exp(-5.88*(t));
```

```
48
49 k=plot(t,i,'m');
50 xlabel('Root brine fraction');
51 ylabel('Strength [MPa]');
```

Timco and Frederking (1990) and Moslet (2007) compared compressive strength to total porosity, curve fits based on the data from this work is based on the Matlab code:

```
1 function [fitresult, gof, fitresult1, gof1] = createFit(z, y, z1, y1)
2 clear all
3 close all
4 clc
5
6 load totpor1.dat
7 y= totpor1(:,2);
8 z= totpor1(:,1);
9
10 %% Fit: 'untitled fit 1'.
11 [xData, yData] = prepareCurveData( z, y );
12
13 % Set up fittype and options.
14 ft = fittype( 'A*(1-(x/b)^0.5)^2');
15 opts = fitoptions( ft );
16 opts.Display = 'Off';
17 opts.Lower = [-Inf 0];
18 opts.StartPoint = [5 100];
19 opts.Upper = [Inf  1000];
20
21 % Fit model to data.
22 [fitresult, gof] = fit( xData, yData, ft, opts )
23
24 plot( fitresult,'g', xData, yData,'r.' );
25 hold on;
26
27 % Plot fit with data.
28 load totpor.dat
29 y1= totpor(:,1);
30 z1= totpor(:,2);
31
32 %% Fit: 'untitled fit 1'.
33
34 [xData1, yData1] = prepareCurveData( z1, y1 );
35
36 % Set up fittype and options.
37
38 ft1 = fittype( 'A1*(1-(x/b1)^0.5)^2');
39 opts = fitoptions( ft1 );
40 opts.Display = 'Off';
41 opts.Lower = [0 0];
42 opts.StartPoint = [20 100];
43 opts.Upper = [Inf  1000];
44
45 % Fit model to data.
```

```
46
47  [fitresult1, gof1] = fit( xData1, yData1, ft1, opts )
48  plot(fitresult1,'b', xData1, yData1,'b.');
49  hold on
50
51  d=10:1:250;
52  i=8*(1-(d/270).^0.5);
53  plot(d,i,'m')
54  hold on
55  e=30:1:170;
56  j=35*(1-(e/200).^0.5);
57  plot(e,j,'k')
58  hold on
59
60  l=24*(1-(d/700).^0.5).^2;
61  plot(d,l,'c');
62  hold on
63
64  m=8*(1-(d/700).^0.5).^2;
65  plot(d,m,'r--');
66  axis([0 300 0 10]);
67
68  xlabel( 'Total porosity [ppt]' );
69  ylabel( 'Compressive strength [MPa]' );
70  set(0,'DefaultAxesFontSize',14);
```

A.2.2   Curve fitting E(z)

With this curve fit the data of elastic modulus in table 7 are fitted to equation 63.

```
1  function [fitresult, gof, fitresult1, gof1, fitresult2, gof2] =
2  createFit2(z, y,z1,y1,z2,y2)
3
4  clear all
5  close all
6  clc
7
8  % ice thickness is h=0.7 for all curve fits
9  % fitting alfa and E for n=0.5, n=1, n=2
10 %%%%%%%%%%%%%%%%%%%%% n=0.5 %%%%%%%%%%%%%%%%%%%%%%%%%%%%%%
11 z =[ 0.1000 0.1000 0.1000 0.2850 0.2850  0.5050 0.5050 0.5050];
12 y =[177 156 150 107 92 74 58 57];
13
14 [xData, yData] = prepareCurveData( z, y );
15
16 % Set up fittype and options.
17 ft = fittype( 'E*(1-(1-a)*(x/0.7+(0.5+2*a)*(0.5+1)
18 /2/(0.5+2)/(0.5+a))^(0.5))','independent', 'x', 'dependent', 'y' );
19
20 opts = fitoptions( ft );
21 opts.Display = 'Off';
22 opts.Lower = [0 0.1 ];
23 opts.StartPoint = [0.9706 0.957166948242946];
```

```matlab
24  opts.Upper = [Inf Inf];
25
26  % Fit model to data.
27
28  [fitresult, gof] = fit( xData, yData, ft, opts );
29
30  %%%%%%%%%%%%%%%%%%%%%% n=1 %%%%%%%%%%%%%%%%%%%%%%%%%%%%%%
31  z1 =[ 0.1000 0.1000 0.1000 0.2850 0.2850  0.5050 0.5050 0.5050];
32  y1 =[177 156 150 107 92 74 58 57];
33
34  [xData1, yData1] = prepareCurveData( z1, y1 );
35
36
37
38  % Set up fittype and options.
39  ft1 = fittype( 'E1*(1—(1—a1)*(x/0.7+(1+2*a1)*(1+1)
40  /2/(1+2)/(1+a1))^(1))','independent', 'x', 'dependent', 'y' );
41
42  opts = fitoptions( ft1 );
43  opts.Display = 'Off';
44  opts.Lower = [0 0.1 ];
45  opts.StartPoint = [0.9706 0.957166948242946];
46
47  opts.Upper = [Inf Inf];
48
49  % Fit model to data.
50  [fitresult1, gof1] = fit( xData1, yData1, ft1, opts );
51
52
53
54  %%%%%%%%%%%%%%%%%%%%%% n=2 %%%%%%%%%%%%%%%%%%%%%%%%%%%%%%
55  z2 =[ 0.1000 0.1000 0.1000 0.2850 0.2850  0.5050 0.5050 0.5050];
56  y2 =[177 156 150 107 92 74 58 57];
57
58  [xData2, yData2] = prepareCurveData( z2, y2 );
59
60  % Set up fittype and options.
61  ft2 = fittype( 'E2*(1—(1—a2)*(x/0.7+(2+2*a2)*(2+1)
62  /2/(2+2)/(2+a2))^(2))', 'independent', 'x', 'dependent', 'y' );
63
64  opts = fitoptions( ft2 );
65  opts.Display = 'Off';
66  opts.Lower = [0 0.1 ];
67  opts.StartPoint = [0.9706 0.957166948242946];
68  opts.Upper = [Inf Inf];
69
70  % Fit model to data.
71  [fitresult2, gof2] = fit( xData2, yData2, ft2, opts );
72
73
74  %%%%%%%%%%%%%%%%%%%%%%PLOT all curve fits %%%%%%%%%%%%%%%%%%%%%%%%
75  figure( 'Name', 'untitled fit 1' );
76  plot( fitresult,'g', xData, yData);
77  hold on
78  plot( fitresult1,'b', xData1, yData1);
79  hold on
```

```
80  plot( fitresult2,'r', xData2, yData2);
81  legend('E(z)', 'n = 0.5', 'E(z)','n=1','E(z)','n = 2',
82     'Location', 'NorthEast' );
83  xlabel( 'z' );
84  ylabel( 'E(z)' );
85  fitresult1
86  fitresult2
```

A.2.3 Stress distribution with E(z), Svea

This code is for the stress distribution across the thickness of beam C3. By changing the first the boundary conditions this Matlab code can be used to obtain stress distributions for all beams with E(z) and flexural strengths given in table 21. The plot in figure 45, is found from this Matlab code, it plots the stress distribution across the ice thickness.

```
1   clc
2   close all
3   clear all
4   format long
5
6   %boundary conditions
7   h=0.73;   %[m];
8   L=3.17; %[m]
9   b=0.70; %[m]
10  F=4371; %[N]
11
12  %curvefit n=0.5
13  n=0.5;
14  E=381.5e6;%[Pa]
15  a=0.1862;
16
17  n1=1.0;
18  E1=252.6e6;
19  a1=0.3059;
20
21  n2=2.0;
22  E2=187.2e6;
23  a2=0.4691;
24
25  z0=(h*(n+2*a)*(n+1))/(2*(n+2)*(n+a));
26  E_top=  E.*(1-(1-a).*(-z0/h+z0/h).^n); %[pa];
27  fun = @(z) E.*(z.^2).*(1-(1-a).*(z/h+z0/h).^n);
28  I=b* integral(fun,-z0,(h-z0)) % [N*m^2]
29  sigmaEz=F*L*z0*E_top/I
30  sigma=(6*F*L)/(b*h^2)
31  diff=sigma/sigmaEz
32
33  z=-z0:0.05:(h-z0);
34  Ez= -z*E.*(1-(1-a).*(z/h+z0/h).^n);
35  sig=F*L*Ez/I;
36  plot(sig,z,'r')
```

```matlab
37  hold on
38
39  %curvefit n=1.0
40  z01=(h*(n1+2*a1)*(n1+1))/(2*(n1+2)*(n1+a1))
41  E_top1=  E1.*(1-(1-a1).*(-z01/h+z01/h).^n1) %[pa];
42  fun1 = @(z) E1.*(z.^2).*(1-(1-a1).*(z/h+z01/h).^n1);
43  I1=b* integral(fun1,-z01,(h-z01)) % [N*m^2]
44  sigmaEz1=F*L*z01*E_top1/I1
45  diff1=sigma/sigmaEz1
46
47  z1=-z01:0.05:(h-z01);
48  Ez1= -z1*E1.*(1-(1-a1).*(z1/h+z01/h).^n1);
49  sig1=F*L*Ez1/I1;
50  plot(sig1,z1,'b')
51  hold on
52
53  %curvefit n=2.0
54  z02=(h*(n2+2*a2)*(n2+1))/(2*(n2+2)*(n2+a2))
55  E_top2=  E2.*(1-(1-a2).*(-z02/h+z02/h).^n2) %[pa];
56  fun2 = @(z) E2.*(z.^2).*(1-(1-a2).*(z/h+z02/h).^n2);
57  I2=b* integral(fun2,-z02,(h-z02)) % [N*m^2]
58  sigmaEz2=F*L*z02*E_top2/I2
59  diff2=sigma/sigmaEz2
60
61  z2=-z02:0.05:(h-z02);
62  Ez2= -z2*E2.*(1-(1-a2).*(z2/h+z02/h).^n2);
63  sig2=F*L*Ez2/I2;
64  plot(sig2,z2,'m')
65  hold on
66
67  sigma=6*F*L/b/(h^3)*-z2;
68  plot(sigma,z2,'k');
69  xlabel('Stress Pa');
70  ylabel('z [m]');
71  grid on;
```